Phase separation in $Y_{.63}Ca_{.37}TiO_3$

Masterthesis

II. Physikalisches Institut der
Universität zu Köln

submitted by

Bernhard Zimmer

in July 2015

Advisor: Prof. Dr. Ir. Paul H. M. van Loosdrecht
Second advisor: Prof. Dr. Markus Grüninger

DECLARATION OF AUTHORSHIP

I, Bernhard Zimmer, hereby declare that this thesis is my own work and that all resources used in this work are mentioned in the references.

Cologne, July 14, 2015   *Bernhard Zimmer*

ACKNOWLEDGEMENTS

CONTENTS

LIST OF FIGURES

ABSTRACT

In this work the results of optical microscopy and Raman spectroscopy measurements conducted on $Y_{.63}Ca_{.37}TiO_3$, which features temperature driven metal-insulator transition are presented. Optical microscope pictures exhibit dark and bright domain patterns on the surface with length scales of orders several to a hundred micrometer. The observed temperature evolution of the domains exhibit a percolation transition of the domains and identification of the dark domains with metallic phase and bright domains with insulating phase is consistent with the temperature behaviour of the resistivity of the material. Using micro-Raman spectroscopy it is possible to study the two domains separately. There is a clear difference in the Raman spectra between the two domains for $T \lesssim 150\,\text{K}$: in the bright domains the Raman signal of insulating samples near x_{MIT} is obtained, whereas the Raman spectra of the dark domains correspond to those of metallic samples, confirming the assignment of the domains. The results of the experiments on $Y_{.63}Ca_{.37}TiO_3$ therefore yield existence of phase separation between metallic and insulating phases of macroscopic domain size, with the insulator-metal transition being caused by a percolation transition of the metallic phase.

1. INTRODUCTION

Transition metal oxide (TMO) compounds exhibit a large variety of phenomena concerning the electronic properties of these materials, such as metal-insulator transition (MIT), colossal magneto resistance effect (CMR), high-temperature superconductivity (HTSC) or phase separation (PS), to mention a few prominent effects [1]. The understanding of these electronic effects in the TMOs often exceeds the simple single-particle band picture or even the simple Hubbard model and one must in principle take into account the interplay of charge, spin, orbital and lattice degrees of freedom (d.o.f.). This leads to a competition of different energy scales associated with each d.o.f. and the interplay among them, which in turn can give rise to rich phase diagrams of TMOs, as *e.g.* shown in fig. 1.1, which represents the phase diagram of a cuprate like $La_{2-x}Sr_xCuO_4$. A good and extensive introduction to the physics of TMO materials can be *e.g.* found in [2].
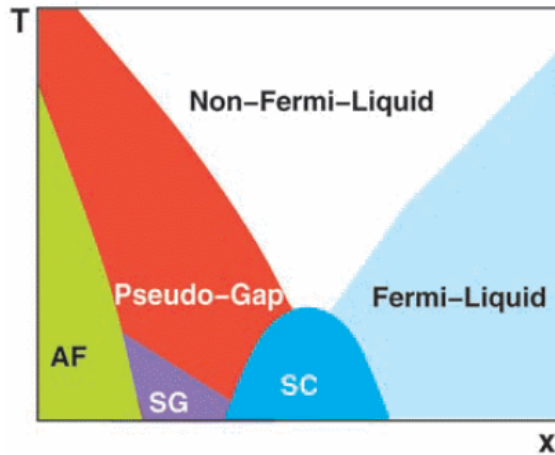
Fig. 1.1: Example of a generic phase diagram of a HTSC. Depending on doping x or temperature T, different phases are stable, like AF = antiferromagnetic phase, SC = superconducting phase, SG = spin glass phase and the other non-abbreviated phases[1].

For the development of potential technical applications, in general a broader and deeper understanding of the physics of TMOs is pursued. Due to the complexity given by the number of d.o.f., the study of simple model systems are of interest. In this context, the doping series of $Re_{1-x}A_xTiO_3$ (Re: rare earth ion, A: alkaline earth ion) are very interesting. The complexity in this system is dramatically reduced as its electronic properties are determined by the $3d^1$

electron of the Ti^{3+}-ion only and the structure is understood by distortion of a simple cubic perovskite structure. Furthermore it is quite easy to manipulate the electronic properties of the system. The electronic bandwidth can be controlled by varying the Re^{3+}-ionic radius and hole doping with A^{2+}-ions enables to drive filling control MITs (FC-MIT) in these systems [3]. But despite the reduced complexity, this material class exhibits already interesting phenomena and rich phase diagrams (see fig. 1.2). Considering in particular the $Y_{1-x}Ca_xTiO_3$ series, the undoped parent compound exhibits an insulating ferromagnetic groundstate. This is rather unusual as ferromagnetism in TMOs is typically accompanied by a metallic state, like *e.g.* in the manganites. Hole doping leads to FC-MIT at rather high doping level of $x_{MIT} = 40\%$ and close to it at $x \approx 33\%$-39% another MIT by varying temperature is observable (see fig. 1.3). This temperature driven MIT is rather unusual, as the material in this doping range is metallic at low temperatures and insulating at high temperatures, as it is seen in the resistivity. Usually the opposite is expected and most MITs observed in varying temperature are opposite in direction like in vanadium oxides [4], with the insulating phase being stable at lower temperatures and a transition to a metallic phase at higher temperatures. A pure phase transition from a metallic to insulating state with varying temperature however is expected to give a rather sharp jump in the resistivity around the transition temperature. As it is seen in $Y_{.63}Ca_{.37}TiO_3$ (fig. 1.3) the temperature range where the resistivity changes anomalously is very broad. The observation of phase segregation in this material [5], leads to the suggestion, that the T-driven MIT is driven by percolation of the phases [6]. Although the doping series of $Y_{1-x}Ca_xTiO_3$ has been already subject to extensive research, there are still open questions regarding the nature of this peculiar T-driven MIT. Especially the question why the metallic phase is the stable state at low temperatures remains an open question.
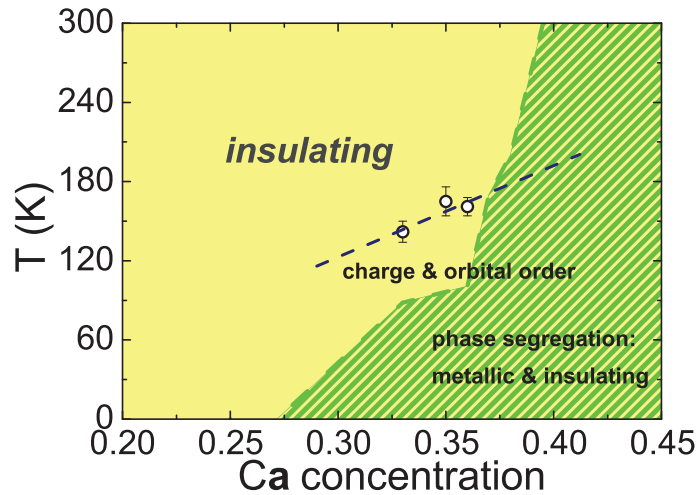
Fig. 1.2: The doping-temperature phase diagram of $Y_{1-x}Ca_xTiO_3$ [7].
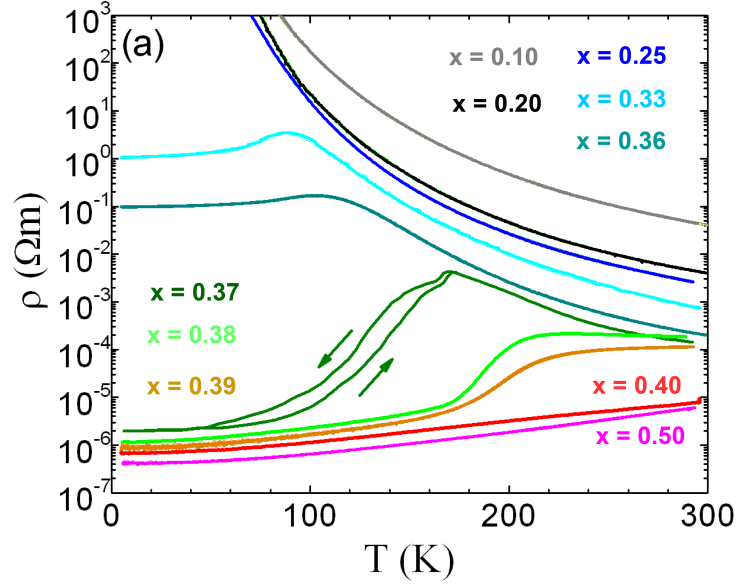
Fig. 1.3: The resistivity of the doping series of $Y_{1-x}Ca_xTiO_3$, exhibiting a MIT by doping and by temperature in the doping range of $x \approx 33\%$-39% [8].

In this work, single crystals of $Y_{.63}Ca_{.37}TiO_3$ grown by A.C. Komarek [8] (ACK083) are investigated to obtain more information on the phase separation in this material and the associated T-driven MIT. Optical microscopy is used to directly observe the phase separation in this material and micro Raman spectroscopy is used to study the influence of the lattice d.o.f. in this system and its possible influence on the electronic properties.

This thesis is outlined as follows: In chapter 2, the basic physics which are of importance for the $Y_{1-x}Ca_xTiO_3$ material are briefly reviewed. As the material is investigated by Raman spectroscopy, this spectroscopic method is described in more detail in chapter 3, where also the experimental setup used for the measurements is described. In chapter 4 the analysis and discussion of the obtained data of the $Y_{.63}Ca_{.37}TiO_3$ measurements are presented. Finally a short summary of this work and outlook to open questions can be found in chapter 5.

2. PHYSICS OF THE TITANATES AND PHASE SEPARATION IN TMOS

2.1 Physics of the Titanates

To understand the electronic properties of $Y_{1-x}Ca_xTiO_3$, it is instructive to consider first the properties which determine the electronic groundstate of the parent compound $YTiO_3$.

Using the electronic single particle picture, $ReTiO_3$s would be expected to be metallic, since the $3d^1$-electron of the Ti^{3+} ion would give rise to a partially filled band. The insulating groundstate of $ReTiO_3$s is ascribed to be a fingerprint of electron electron correlation, where the hopping of the Ti-$3d^1$-electron is penalized by the on-site Coloumb energy and they are classified as Mott insulators [3, 9].

Structurally in the sense of close packing spheres, the mismatch of the ionic radii of the constituents give rise to a distorted perovskite structure of orthorhombic symmetry *Pbnm*, the so called $GdFeO_3$ structure [10]. It is especially induced by cooperative rotation and tilts of the corner-sharing TiO_6 octahedra [11]. Especially the mismatch of Re^{3+}- and Ti^{3+}-ionic radii leads to a decrease of the Ti-O-Ti bond angles from 180°, which decreases the more, the smaller the Re^{3+}-ionic radius is. A decrease of the Ti-O-Ti bond angle from 180° leads to a decrease in orbital overlaps and a corresponding decrease of the electronic bandwidth and superexchange interaction. Concomittant with the superexchange interaction is a magnetic ordering at lower temperatures of the $ReTiO_3$s, which in the case of $YTiO_3$ leads to an insulating ferromagnetic groundstate [12]. In accordance with the GKA-rules [13–15], antiferro-orbital ordering with associated Jahn-Teller distortion of the TiO_6 octahedra is also present.

Doping $ReTiO_3$ with A^{2+}-ions (usually Sr^{2+} or Ca^{2+}) corresponds to putting hole-carriers into the system and eventually renders the groundstate metallic. In the $Y_{1-x}Ca_xTiO_3$ series, first the ferromagnetic ordering vanishes at $x_{FP} \approx 15\%$, leading to a paramagnetic groundstate concomitant with a weakening of the orbital order [16]. The vanishing of the magnetic order is expected, as spins are removed from the system via hole doping. Whereas $La_{1-x}Sr_xTiO_3$ becomes metallic at $x_{MIT} = 5\%$, the transition to a metallic groundstate in $Y_{1-x}Ca_xTiO_3$ occurs at unexpected high doping level of $x_{MIT} = 40\%$ [8, 9]. Furthermore in doping ranges of $x \approx 33$-39% a drop of the resistivity towards low temperatures is observed, leading to a temperature driven metal-insulator transition (T-driven MIT), where the material is metallic at low temperatures and insulating at high temperatures (fig. 1.3). This ordering of electronic phases along temperature is rather
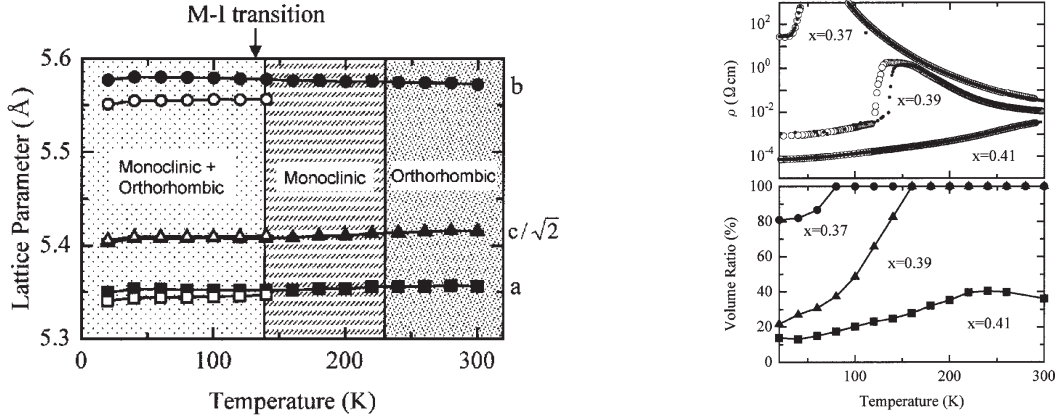
Fig. 2.1: Left: Temperature evolution of the crystal structure in $Y_{.61}Ca_{.39}TiO_3$. Right: Direct comparison of the electrical resistivity and volume ratio of the LTM phase. Both taken from [16].

uncommon and this T-driven MIT is connected to the structural temperature evolution of the material [5, 8], which is shown in fig. 2.1, left. Going down in temperature, first a structural phase-transition from orthorhombic *Pbnm* (HTO = high temperature orthorhombic) to monoclinic $P2_1/n$ (LTM = low temperature monoclinic) symmetry around 200 K takes place. This transition exhibits no features in the resistivity data, meaning both phases HTO and LTM are insulating. The LTM phase is suggested to be charge and orbitally ordered, explaining the stability of the insulating phase w.r.t. doping and a corresponding high x_{MIT} and is associated with a G-type distortion of the octahedra [7, 8]. Fig. 2.2 shows the pattern of the G-type distortion which consists of alternating expanded and contracted TiO_6 octahedra. At lower temperatures below 200 K, a new orthorhombic *Pbnm* (LTO) phase starts to coexist next to the LTM phase and the volume fraction of the LTO phase increases with decreasing temperature (depicted exemplary for a $x = 39\%$ sample in fig. 2.1, left). This volume fraction behaviour resembles the resistivity data, identifying the LTO phase as the metallic phase and the T-driven MIT is suggested to be caused by percolation of the LTO phase (see fig. 2.1, right) [5, 6, 17]. The LTO and HTO phases have the same crystallographic symmetry *Pbnm*, but they differ in their lattice parameters (see fig 2.1, left), with the LTO unit cell being smaller. It should be emphasized here, that the phase separation still takes place in metallic samples ($x > 40\%$), meaning that the volume fraction of the LTO phase is high enough even at room temperature to render these samples metallic, coexisting next to small fractions of the insulating LTM or HTO phase (as is also seen in fig. 2.1, right). For a better overview of the structural temperature evolution and its dependency on doping level x in $Y_{1-x}Ca_xTiO_3$, the phase diagram is shown in fig. 1.2.

Substitution of Y^{3+} ion by smaller Er^{3+} or Lu^{3+} ions in $Re_{1-x}Ca_xTiO_3$, is expected to stabilize the insulating properties of the system. An increase of x_{MIT} as seen in resistivity measurements (see fig. 2.3) and observed enhancement of the G-type distortion associated with charge and orbital order of the LTM phase, confirms the enhanced stability of the insulating phase by sub-

stituting for smaller Re-ions [7].
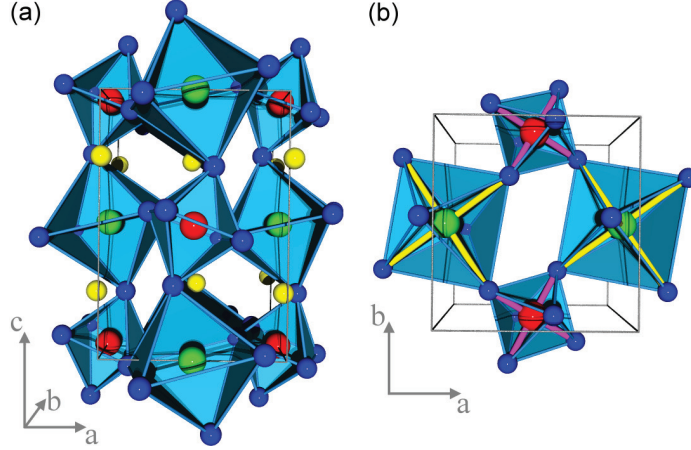
Fig. 2.2: (a-b) Visualisation of the G-type distortion in the LTM phase with alternating expanded and contracted octahedra [8].
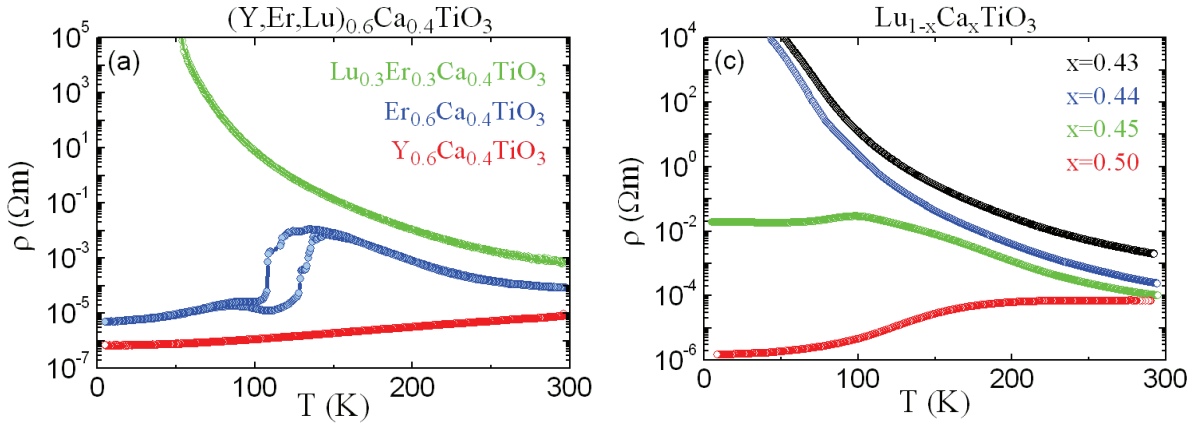
Fig. 2.3: Resistivity data of $Re_{1-x}Ca_xTiO_3$ with different Re-ionic radii, which shows the stabilization of the insulating properties with decreasing Re-ionic radius [7].

The ordering of the electronic phases with the metallic phase being more stable at lower temperatures is rather unusual. To qualitatively explain this statement, the free energy F is considered:

$$F = U - TS \tag{2.1}$$

with U being the internal energy and S the entropy of an electronic phase. With increasing temperature, the entropy becomes more and more decisive (second term in eq. 2.1) and even-

tually the system goes into the higher entropy state [2]. As an insulating state is usually the more ordered state in comparison to the metallic state, MITs usually exhibit the transition from insulating to metallic phase with increasing temperature. However the opposite behaviour in $Re_{1-x}Ca_xTiO_3$ (Re = Y,Er,Lu) suggest, that the metallic state is here the lower energy state w.r.t. U and the insulating phase exhibits a higher entropy. A charge order scenario away from $x = 50\%$ doping could account for such an entropy contribution, even at $T = 0\,K$. Charge ordering for $x = 50\%$ doping results in a perfect checkerboard pattern. Away from $x = 50\%$ doping, the remaining electrons have to fill the holes of the underlying checkerboard pattern, giving rise to a corresponding increase of number of available states and increase in entropy. Similar reasoning is used to explain the phase diagrams in $V_{2-x}Cr_xO_3$ and $Pr_{1-x}Ca_xMnO_3$, where also metallic to insulating phase transitions occur with increasing temperature [2, 18].

2.2 Phase separation in TMOs

Since the T-driven MIT and the phase separated state are closely connected in $Y_{1-x}Ca_xTiO_3$, phase separation is considered in more detail in the following. There exist several sources and mechanisms explaining phase separation scenarios. Electronic phase separation, where the charge density of the coexisting phases differ, lead to nanoscale (=microscopic) domain sizes, due to the Coulomb interaction of the charge carriers [2]. The length scales of domains in $Y_{1-x}Ca_xTiO_3$ ranging from half a micrometer to one hundred micrometer observed by TEM [17] and in this work therefore suggest a different origin of the phase separated state. Of interest are therefore mechanisms which could give rise to macroscopic phase separation. Disorder and strain are in this context the most important factors, influencing the phase separated state, which is described in more detail in the following.

- **Quenched Disorder:** The coexistence of two phases can be generated by a relatively simple model, which is the Random Field Ising Model (RFIM) defined by:

$$H = -J \sum_{\langle ij \rangle} S_i S_j - \sum_i h_i S_i. \tag{2.2}$$

  In the context of this work, eq. 2.2 would be read as the following: the index i counts the unit cells in the system, $S_i = \pm 1$ represents the metallic (LTO) or insulating (LTM) phase. The exchange J between the S_i accounts for the clustering of the phases and $\langle ij \rangle$ refers to next nearest neighbour summation. To take into account the disorder in the system generated by the Ca doping, random fields $\{h_i\}$ are introduced. Since the Y^{3+} and Ca^{2+} ionic radii differ, the h_i mimic local fluctuations in the hopping amplitude t of the charge carriers. The strength of the disorder is determined by the interval $[-W,W]$, where $\{h_i\}$ is drawn from.Without disorder ($\{h_i\} \to h$), the (Ising) Hamiltonian of eq. 2.2 has a first

order phase transition at $h = 0$, which gets smeared out introducing disorder. This then can lead to generation of bubbles of the competing phase within the predominant phase. The energy cost generated by the domain wall has to be compensated by the disorder within the bubble. The main results of simulations using eq. 2.2 are that when decreasing the disorder W, the domain sizes of the phases increase. Applying an external field $H_{ext} \sum_i S_i$ or lowering the temperature at zero field leads to a percolation transition [19].

- **Strain:** A model based on strain and lattice distortions is used to describe multi-scale phase separation in the manganites [20]. In this model the competition of a distorted phase with an undistorted phase is described considering their energies w.r.t. strain and distortions. The distorted phase is the global energy minimum state whereas the undistorted phase corresponds to the local minimum state (see fig. 2.4). Such a description would be compatible with the TEM observations of the LTO phase being highly distorted compared to the LTM phase in $Y_{1-x}Ca_xTiO_3$ [17]. Stable coexistence between both states requires a sufficiently high energy barrier ΔE between both states. What this model shows is that apart from the Peierls-Nabarro energy barrier, which is known for the stabilization of dislocations, the strain itself in the system contributes to the stability of the phase separated state. For more details on this model see [20].

Inherent strain and lattice distortion effects to phase separation play also an important role in martensitic transitions [18, 21, 22]. It essentially refers to a cooperative atomic motion producing a different crystal structure (=martensite) within the parent crystal, giving at first rise to strain in the parent crystal (=accommodation strain) and thereby has a lot in common with the model described above. The growth of the martensite and the phase separated state is strongly influenced by the accommodation strain. Usually this strain increases upon cooling which leads to an thermo-elastic equilibrium between the coexisting phases. Micrometer large domains of lenticular shapes, hysteresis in resistivity, growth of martensite with time, domain size dependency on grain size in polycrystals (the smaller the grains the more difficult the strain can be accommodated) are observations in the manganites interpreted by the martinsitic picture.
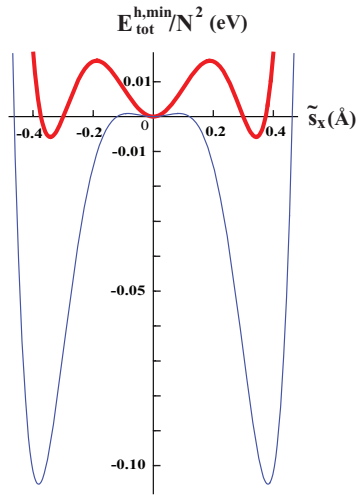
Fig. 2.4: Energy landscape w.r.t. distortion s_x in case of homogenous ground state. The energy barrier ΔE in the red curve between local and global minima is huge enough to generate phase separated states [20].

3. RAMAN SPECTROSCOPY

Inelastic light scattering in solids probed by optical Raman spectroscopy can provide various information about a material's properties. Raman spectra are sensitive to the symmetry of the material, making it possible to monitor structural phase transitions along varying temperature, pressure or other parameters. Furthermore the energies of excitations like phonons, magnons or other collective excitations in the material are directly obtained. Using single crystals it is also possible to obtain symmetry information of the excitations. This possibility to examine excitations makes Raman spectroscopy a powerful tool to gain insight in a material's properties associated with the examined excitations. One of the most common applications of Raman spectroscopy in condensed matter physics is to investigate the lattice degree of freedoms, that is the phonon and the structural temperature evolution in a material. In sec. 3.1 this is described in more detail, as the Raman investigations in this work focuses also on the lattice d.o.f. The explicit modelling of Raman data for this work is described in sec. 3.2 and the experimental setup used for the Raman measurements is described in sec. 3.3. At the end of this chapter, in sec. 3.4 Raman data on $Y_{1-x}Ca_xTiO_3$ which are of interest for this work are shown. For more extended information on Raman spectroscopy in solids see *e.g.* [23] or [24].

3.1   Theory of Raman spectroscopy

In the following the Raman effect involving inelastic scattering of photons in matter by phonons is considered. The energy transfer in the Raman process (see Eq. 3.1), where the energy ω of a phonon is added or subtracted to the energy ω_I of the incoming light, depending on if the phonon is destroyed (Anti-Stokes process) or generated (Stokes process), can be inferred from probing the generated Raman light with energy ω_S, if ω_I is known. Momentum conservation requires the momentum difference of incident ($\boldsymbol{k_I}$) and scattered ($\boldsymbol{k_S}$) light to equal the phonon momentum $\boldsymbol{q}$ (see eq. 3.2 and fig. 3.1).

$$\omega_S = \omega_I \pm \omega \tag{3.1}$$

$$\boldsymbol{k_S} = \boldsymbol{k_I} \pm \boldsymbol{q} \tag{3.2}$$
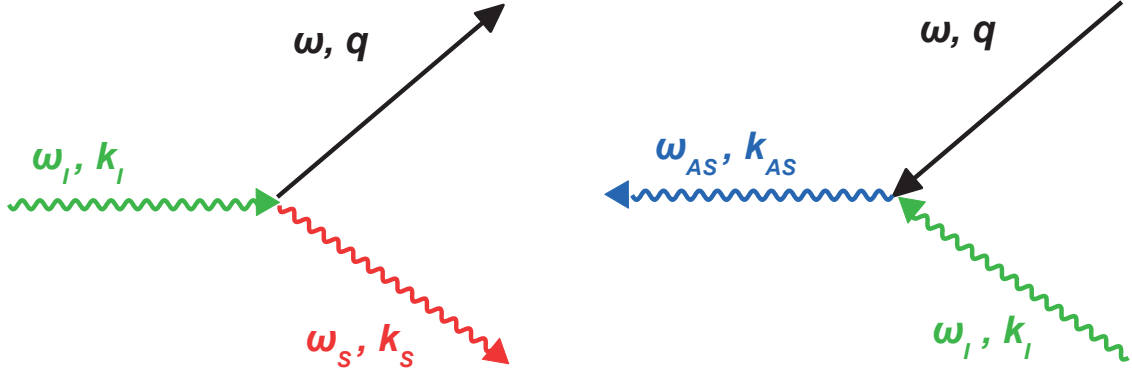
Fig. 3.1: Raman scattering processes drafting momentum conservation with curvy lines representing photons and straight lines phonons. Left: Stokes process. Right: Anti-Stokes process.

Since the energy of the photons used for Raman spectroscopy is typically in the optical regime the momentum $|\boldsymbol{k_I}|$ carried by the light which can be transferred to a phonon is very small compared to the wavevectors at the Brillouin zone edge ($\sim 1/1000$). Thus the phonons participating in the Raman process can be considered to have zero momentum.

In a classical picture, the Raman light can be described to be generated by local variations in the electric polarizability tensor χ of the material. These variations arise due to lattice vibrations which are described by normal coordinates $Q = Q_0 \cos(\omega t)$. The polarizability tensor χ is then a function of the normal coordinates and can be correspondingly Taylor expanded w.r.t. Q: $\chi(Q) = \chi_0 + \frac{\partial \chi_0}{\partial Q} Q + ...$ An electric field $\boldsymbol{E}(t) = \boldsymbol{E_0} \cos(\omega_I t)$ in matter gives rise to a polarization field $\boldsymbol{P} = \epsilon_0 \chi \boldsymbol{E}(t)$. Taking into account the local variations in χ via the expansion w.r.t. Q, the polarization field reads:

$$\boldsymbol{P} = \epsilon_0 \boldsymbol{E_0}(\chi_0 \cos(\omega_I) + \frac{1}{2}\frac{\partial \chi_0}{\partial Q}(\underbrace{\cos(\omega_I + \omega)}_{\boldsymbol{P_{AS}}} + \underbrace{\cos(\omega_I - \omega)}_{\boldsymbol{P_S}}) + ...) \tag{3.3}$$

where it is seen, that the linear expansion term of χ gives rise to the Raman shifts. Of interest is the scattering cross section $\frac{d^2\sigma}{d\Omega d\omega_S}$ of the Raman scattered light which is measured. An explicit expression for the scattering cross section (SCS) is obtained using the Maxwell equations with $\boldsymbol{P_S}$ as source term and applying the fluctuation-dissipation theorem [23]. The result for the Stokes scattered light reads:

$$\frac{d^2\sigma}{d\Omega d\omega_S} = \frac{\hbar\omega_I \omega_S^3 \upsilon V n_S \left| \boldsymbol{\epsilon_S} \cdot \frac{\partial \chi_0}{\partial Q} \boldsymbol{\epsilon_I} \right|^2 \{n(\omega,T) + 1\}}{(4\pi)^2 2c^4 n_I N \omega} g(\omega) \tag{3.4}$$

where $n(\omega,T)$ is the occupation number of the phonon (Bose-Einstein distribution), $g(\omega)$ the phonon lineshape, $\boldsymbol{\epsilon_I}$, $\boldsymbol{\epsilon_S}$ are the polarization vectors of the incoming and scattered light. υ is

the scattering volume, N/V the density of atoms in the material and n_I, n_S denote refractive indices of incident and scattered light respectively.

The SCS section for the Anti-Stokes process is obtained the same way as described for the Stokes-process and yields a similar expression, with the major difference that $\{n(\omega,T) + 1\} \rightarrow n(\omega,T)$. So the ratio of the SCS can be used to obtain the temperature associated with the phonons then:

$$\frac{\frac{d^2\sigma}{d\Omega d\omega_S}}{\frac{d^2\sigma}{d\Omega d\omega_{AS}}} = \frac{\omega_S^3}{\omega_{AS}^3} \frac{n_{AS}}{n_S} \exp\left(\frac{kT}{\hbar\omega}\right) \tag{3.5}$$

Eq. 3.5 shows, that the SCS for the Stokes process is significantly higher at low temperatures compared to the Anti-Stokes process.

In a quantum mechanical treatment the Raman scattering process can be described as a second order process of the light matter interaction and the SCS obtained gives more detailed information about the intensity dependence on the energy of the incident light, including resonance effects. What is of interest here are the symmetry properties of the SCS of the Raman process, giving rise to selection rules. For this it is sufficient here to consider only qualitatively the polarization induced by the Stokes process and corresponding involved transitions of wavefunctions [25, 26]:

$$\langle \boldsymbol{P}_S \rangle \propto \langle f|\boldsymbol{p}|m \rangle \langle m|\boldsymbol{p}|i \rangle \tag{3.6}$$

with $|i\rangle$, $|m\rangle$ and $|f\rangle$ being initial, intermediate and final states respectively and $\boldsymbol{p}$ the electric dipole operator. The wavefunctions include in general the electronic and lattice d.o.f. But at least $|i\rangle$ and $|f\rangle$ can be assumed to be in the electronic ground state, so that only symmetry considerations w.r.t. lattice d.o.f. are relevant. In the following the selection rules of the Raman effect obtained by means of group theory are outlined. For a fuller account on this subject see *e.g.* [26].

From a symmetry point of view, the classical (eq. 3.4) and quantum mechanical (eq. 3.6) descriptions are identical. Both $\frac{\partial \chi_0}{\partial Q}$ and $\boldsymbol{p}\,|m\rangle\,\langle m|\,\boldsymbol{p}$ transform as a second rank tensor. The Raman process by phonons thus is characterized by a second rank tensor, which is usually referred to as the Raman tensor α. This tensor contains the symmetry information of the phonons. Considering the Stokes process, with $|i\rangle$ being in a zero phonon state and $|f\rangle$ being in a single phonon state, the selection rule is determined by $\Gamma_f \subseteq \Gamma_{xy} \otimes \Gamma_i$, with Γ_f, Γ_{xy} and Γ_i being the irreducible representations of $|f\rangle$, α and $|i\rangle$ respectively. $|i\rangle$ in the zero phonon state is fully symmetric, thus the selection rule reads: $\Gamma_f \subseteq \Gamma_{xy}$. Simply spoken this means that the functions describing the phonons which are Raman active, need to transform like the product of coordinates (*e.g.* like $x \cdot y$ or z^2), as the entries of α do. The entries $\boldsymbol{e_i} \otimes \boldsymbol{e_j}$ of α are thus in general associated with a phonon, transforming correspondingly as $\boldsymbol{e_i} \otimes \boldsymbol{e_j}$. Eq. 3.4 shows, how

chosen polarizations of incident and scattered light makes it possible to probe specific entries of the Raman tensor α. Using single crystals it is therefore possible to specifically probe phonons of certain symmetries. The polarization geometry in Raman experiments is commonly abbreviated in the Porto notation:

$$\boldsymbol{k_I}(\epsilon_I \epsilon_S)\boldsymbol{k_S}, \tag{3.7}$$

$\boldsymbol{k_I}$ and $\boldsymbol{k_S}$ being the wavevector directions of the incident and scattered light respectively. Usually the crystal axes of the sample are used as the coordinate system. As the phonons involved in the Raman process are approximately $\boldsymbol{k} = 0$ phonons, it is the symmetry of the Brillouin-zone-Γ-point, that is the full point group associated with the space group of the material, which determines the symmetry properties of α.

A classification of the phonons of a material of known space group is usually achieved via a normal mode decomposition of the $\Gamma = 0$ phonons, that is the determination of the number and symmetry of the (Raman, Infrared active and silent) phonons. This is done using group theory and a description of such methods can be found *e.g.* in [26] or [27]. The normal mode decompositions can be looked-up in [28], where it is only necessary to know the occupation of the Wyckoff positions to obtain the correct number of the modes. In [28] the modes are listed according to a nuclear site group analysis, which means for each mode it is apparent which Wyckoff position is involved. As an example, the normal mode decomposition of YTiO₃ using [28] is outlined in the following. Fig. 3.2 left shows the character table of the point group associated with the *Pbnm* space group. In this table, basis functions of coordinate products like xy etc. indicate the irreducible representations Γ, which correspond to Raman active modes. The irreducible representations Γ are abbrevated with capital letters A and B here, which on one hand means non-degeneracy of a mode in energy and on the other hand is a symmetry designation. A stands for totally symmetric, that is the vibrational pattern maintains the symmetry of the material, whereas B_1 *e.g.* stands for a vibrational pattern, which is antisymmetric w.r.t. to a certain rotation. Subscripts g and u designate the parity of the modes. The polarization geometry required to probe a mode of a certain Γ can be either read off from the form of the basis functions or read off from the Raman tensors (see. fig 3.2, right-top). Finally the number of expected Raman modes are listed in the table shown below the Raman tensors (fig. 3.2, right-bottom). This table lists how many modes are generated by a specific Wyckoff position and sorts the modes according to their symmetry. It shows, that only Wyckoff positions $4(c)$ and $8(d)$ participate in Raman active modes. The occupation of the Wyckoff positions in YTiO₃ is obtained from [29], which reads: Y on $4(c)$, Ti on $4(b)$, O1 on $4(c)$ and O2 on $8(d)$. Therefore it is seen, that the Ti-ion does not participate in the Raman active vibrations. Since the Wyckoff position $4(c)$ is occupied twice in YTiO₃, the number of the modes generated by it in the table of fig. 3.2 (right-bottom), needs to be multiplied by 2, to obtain the correct number of Raman active modes. The normal mode decomposition of Raman active modes then reads: $\Gamma_{Raman} = 7A_g + 5B_{1g} + 7B_{2g} + 5B_{3g}$,

Information of the Point Group D$_{2h}$ (mmm)

Character Table[1]

D$_{2h}$(mmm)	#	1	2$_z$	2$_y$	2$_x$	-1	m$_z$	m$_y$	m$_x$	functions
A$_g$	Γ$_1^+$	1	1	1	1	1	1	1	1	x^2,y^2,z^2
B$_{1g}$	Γ$_3^+$	1	1	-1	-1	1	1	-1	-1	xy,J$_z$
B$_{2g}$	Γ$_2^+$	1	-1	1	-1	1	-1	1	-1	xz,J$_y$
B$_{3g}$	Γ$_4^+$	1	-1	-1	1	1	-1	-1	1	yz,J$_x$
A$_u$	Γ$_1^-$	1	1	1	1	-1	-1	-1	-1	·
B$_{1u}$	Γ$_3^-$	1	1	-1	-1	-1	-1	1	1	z
B$_{2u}$	Γ$_2^-$	1	-1	1	-1	-1	1	-1	1	y
B$_{3u}$	Γ$_4^-$	1	-1	-1	1	-1	1	1	-1	x

Raman Tensors

	A$_g$			B$_{1g}$			B$_{2g}$			B$_{3g}$		
a	·	·	·	d	·	·	·	e	·	·	·
·	b	·	d	·	·	·	·	·	·	·	f
·	·	c	·	·	·	e	·	·	·	f	·

○ **Raman Active Modes**

WP	A$_g$	A$_u$	B$_{1g}$	B$_{1u}$	B$_{2g}$	B$_{2u}$	B$_{3g}$	B$_{3u}$
4a	·	·	·	·	·	·	·	·
4b	·	·	·	·	·	·	·	·
4c	2	·	1	·	2	·	1	·
8d	3	·	3	·	3	·	3	·

Fig. 3.2: Tables from [28], to look up Raman active modes in YTiO$_3$. Left: Character table of the point group associated with the space group. Right: on the top the Raman tensors are listed and the table below shows the number of Raman active modes, generated by the Wyckoff positions.

in *Pnma* notation. Note that to obtain explicit energies or polarization vectors of the phonons, explicit lattice dynamical calculations have to be performed.

Finally the spectral lineshape of the phonons in Raman spectra shall be considered. Usually the phonon lineshape $g(\omega)$ (eq. 3.4) probed by Raman spectroscopy is a Lorentzian. What is also observed is a Gaussian due to inhomogeneous broadening [25]. Another lineshape occuring in Raman spectra is a so called Fano line, which arises in general from an excitation with a sharp lineshape, interacting with a continuum excitation spectrum. The interference of both excitations gives rise to an asymmetric lineshape and is described by [30]:

$$\frac{(q+\epsilon)^2}{1+\epsilon^2}, \tag{3.8}$$

with ϵ being a reduced energy variable and q the asymmetry parameter. Here the reduced energy is given by $\epsilon = \frac{\omega-\omega_0}{\Gamma/2}$, with ω_0 being a shifted energy of the sharp excitation and Γ its linewidth induced by the interaction. A more detailed theory of the Fano interaction adjusted to the Raman effect takes into account the density of states of the excitation continuum. The lineshape is still given by eq. 3.8 and the asymmetry parameter is given by [24, 31]:

$$q = \frac{T_p/T_e}{\pi V \rho(\omega)} + \frac{R(\omega)}{\pi \rho(\omega)}, \tag{3.9}$$

with T_p and T_e being Raman transition operators of the sharp excitation and excitation continuum respectively, V the coupling parameter between the sharp line and continuum and R and ρ are the real and imaginary part describing the excitation continuum respectively, meaning that ρ corresponds to the density of states of the electronic continuum. Usually in Raman spectra the interference of phonons with an excitation continuum of electrons gives rise to Fano lineshapes. Note that the $q \to \infty$ limit corresponds to a Lorentzian lineshape, whereas a decreasing $|q|$

corresponds to an increase in the asymmetry of the lineshape.

3.2 Modelling

In the following it is described how the Raman measurements in this work are modelled. The measurement data of interest are considered to be basically composed of phonons and the spectra can be modelled by a corresponding sum of phonon lineshapes. Depending on which lineshape fits a specific phonon best, Lorentzian, Gaussian or Fano (*cf.* sec. 3.1) lineshapes are used to model the zone-center phonons. A linear baseline $a \cdot \omega + b$ as simplest approach to model the background behaviour is chosen and subtracted from the spectrum. The model then reads in general:

$$I(\omega) = (1 + n(\omega,T)) \cdot \left(\sum_i \frac{2A_i}{\pi} \cdot \frac{\Gamma_i}{4(\omega - \omega_{0i})^2 + \Gamma_i^2} + \sum_j \frac{A_j}{\sqrt{2\pi}\sigma} \cdot \exp\left(-\frac{1}{2} \left(\frac{\omega - \omega_{0j}}{\sigma_j} \right)^2 \right) \right.$$
$$\left. + \sum_k \frac{A_k}{q_k} \cdot \frac{\left(q_k + \left(\frac{\omega - \omega_{0k}}{\Gamma_k/2} \right) \right)^2}{1 + \left(\frac{\omega - \omega_{0k}}{\Gamma_k/2} \right)^2} \right) - (a \cdot \omega + b)$$

$$(3.10)$$

The first term describes a Lorentzian lineshape with A_i, Γ_i and ω_{0i} being the amplitude, linewidth and center-frequency respectively. A_j, σ_j and ω_{0j} in the second term are the amplitude, width and center-frequency of a Gaussian lineshape respectively. The third term represents a Fano line with A_k, Γ_k, ω_{0k} and q_k being the amplitude, linewidth, center-frequency and asymmetry-parameter respectively. The Fano-line is here scaled by the q-parameter to reduce the error bar in the amplitude obtained by the fits. Furthermore the q-parameter is treated as a constant, assuming that the energy dependant quantities in eq. 3.9 do not significantly change in the energy range of the Raman spectra. Including the Bose-Einstein factor $(1 + n(\omega,T))$ for the Stokes-Raman spectra (see eq. 3.4) takes out the corresponding temperature influence on the spectral weights obtained by the fits. Igor Pro 6.37 is used to fit the Phonon Raman spectra by eq. 3.10.

3.3 Experimental Raman setup

In the following the used Raman setup is described. Also issues regarding the measurement and data processing linked to the used setup are elucidated here. A sketch of the optical beam path and used equipment of the micro-Raman setup, which is aligned in a 180°-backreflection geometry are shown in fig. 3.3. Illustration of the functionality of the spectrometer is sketched in fig. 3.4, which sketches the optical beam path within the used spectrometer.

For the Raman measurements a Cobolt Samba continuous wave DPSS laser of 532.1 nm wavelengths is used as incident light source. Unwanted sidebands of the laserline are removed with a colour filter. The Raman setup is a micro setup, that is the incident laser light is focused via a microscope on the sample. Using a $50x$ magnification objective, the laser spot size can be reduced down to few micrometers. However maximizing the Raman signal usually yields spot sizes which are bigger. Alignment for the measurements in this work yield a laser spot size of $\sim 30\,\mu\text{m}$. To do temperature dependent measurements, the samples are mounted in a Oxford Microstat cryostat, with which the sample can be in principle cooled down to $\sim 4.2\,\text{K}$ using liquid Helium. As the cryostat itself is mounted on a XY-stage, the laser spot can be positioned with a precision of $\pm 2.5\,\mu\text{m}$ on the sample's surface. The scattered light collected from the Raman process is the light which is directed $180°$ w.r.t. the incident light. This means the scattered light follows the beam path of the incident light in opposite direction through the microscope and is directed to the spectrometer via a beamsplitter (see fig. 3.3). Polarization filters are used to establish cross- or vertical-polarized geometries. One is placed within the beam path of the incident light to enhance the quality of its polarization state. A second polarization filter is placed in front of the entrance of the spectrometer to explicitly probe scattered light of a certain polarization. Since the spectrometer is most sensitive to a certain polarization direction, a $\lambda/2$-waveplate is placed right behind this filter, to rotate the polarization of the scattered light correspondingly.

The Raman scattered light is collected and analysed using a Princeton Instruments TriVista triple spectrometer. It is operated in a triple subtractive mode, where the Raman light is effectively dispersed only by one grating. The first two gratings' purpose is to reject stray light to enhance the energy resolution and to be able to probe closer to the laserline. In fig. 3.4 the principle of this filter can be understood by considering an incident beam path, which enters the entrance slit (ES) tilted compared to the aligned beam path drawn in the sketch. Following the tilted beam path, it is seen, that it gets blocked by the second intermediate slit (IS2). To capture an energy range of $\sim 250\,\text{cm}^{-1}$ to $\sim 1500\,\text{cm}^{-1}$, gratings with 900 l/mm for all three stages are used. By rotation of the gratings, the spectrometer can be centred to different energies. Moving the spectrometer, that is the gratings which are driven by step motors between measurements, can lead to slight energy shifts between measurements. The spectrometer position was therefore fixed for the measurements in this work.

The Raman scattered light is detected with a liquid nitrogen cooled CCD camera from Princeton Instruments, model PyLoN:100. Its high sensitivity leads to signals generated by cosmic rays, which need to be removed from the spectra. For this purpose, using the same measurement settings, the spectra are measured at least two times. By comparison of the spectra, it is then possible to identify the random peaks, which do not belong to the Raman spectrum.

The measurement data presented in sec. 4.3 are also cleaned from a background signal. This background exhibited features at $\sim 500\,\text{cm}^{-1}$ and $\sim 630\,\text{cm}^{-1}$ (see fig. 3.5) and are visible in the measurements. The origin of the background is not clear. By focussing the laser spot in air and integrating for several hours with high power, a smooth reference background is obtained. The reference background curve is however only obtained in an energy spectrum from $\sim 250\,\text{cm}^{-1}$ to

$\sim 800\,\mathrm{cm}^{-1}$.
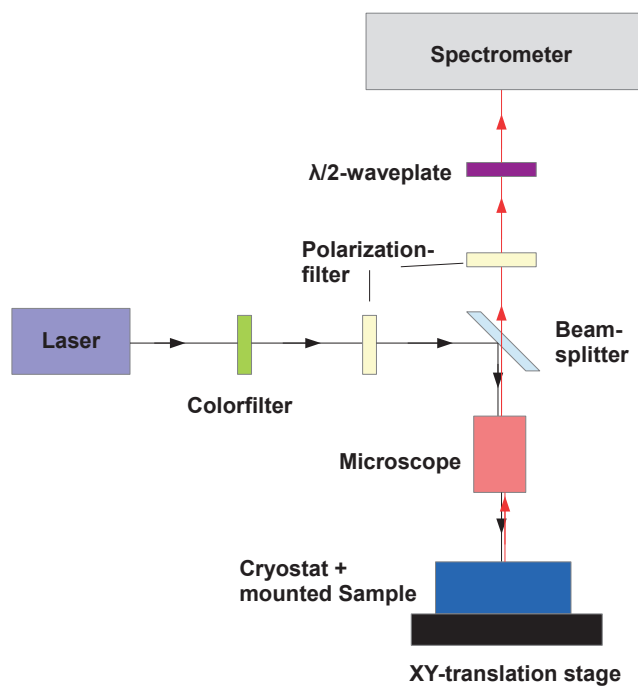
Fig. 3.3: Draft of the optical path of the used Raman setup to illustrate the backreflection geometry. Black beam path corresponds to the incident light and red light corresponds to the beam path of the scattered light.
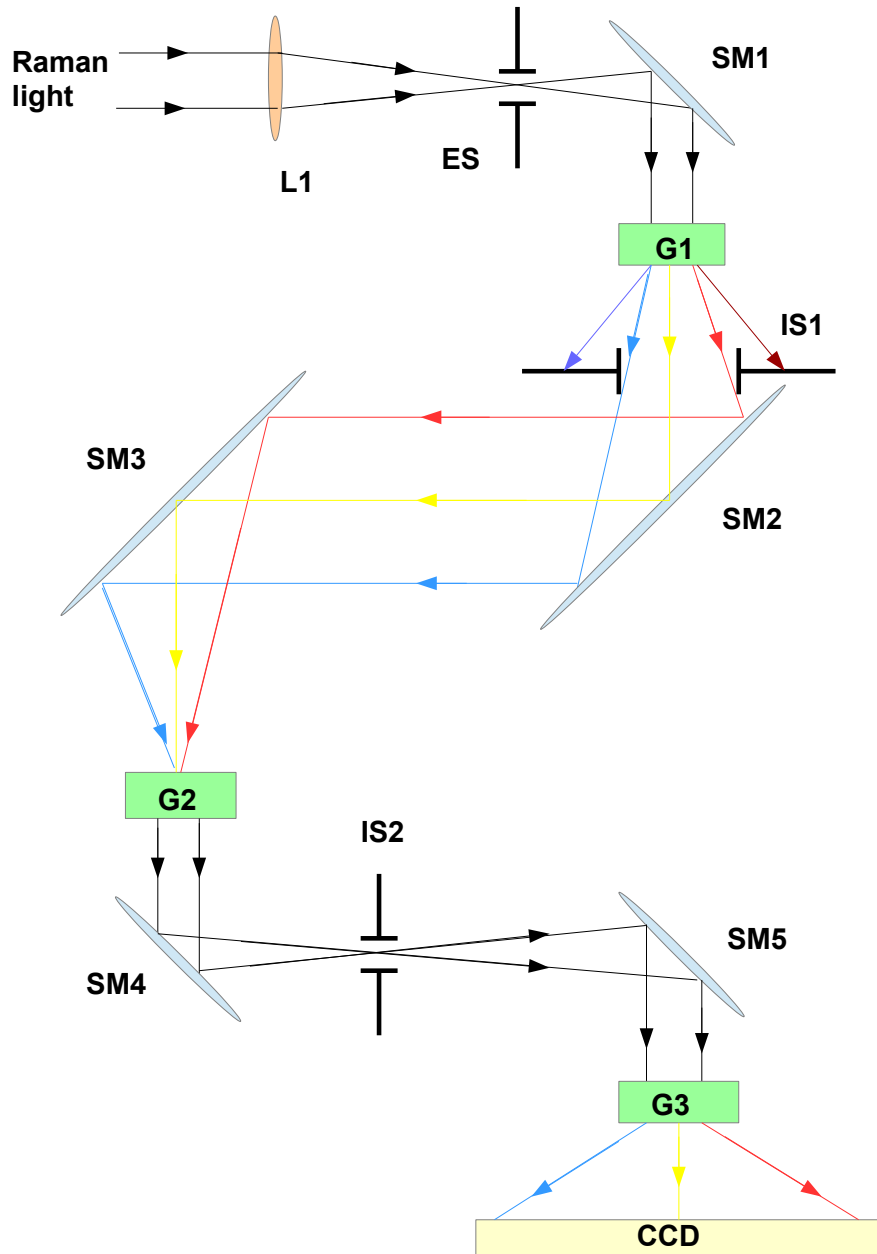
Fig. 3.4: Draft of the optical path of a Raman triple subtractive spectrometer. The Raman light is polychromatic light, which is in the end dispersed on the CCD to give the energy spectrum of the Raman scattered light. The optical elements abbreviated are: L1 = lense; SM1, SM2, SM3, SM4 = spherical mirrors; ES = entrance slit of the spectrometer; IS1 = first intermediate slit to choose the energy range of the Raman spectrum; IS2 = second intermediate slit, which is the slit the ES is optically mapped on to; G1, G2, G3 = gratings.
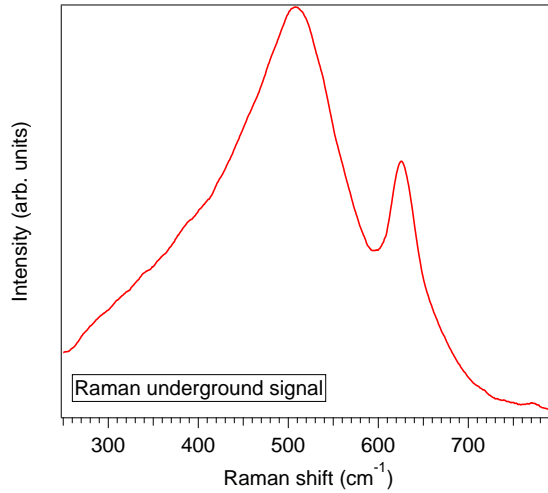
Fig. 3.5: The undergound reference curve for the Raman measurements obtained by focussing the laser spot in air.

3.4   Raman data of doped YTiO3 in literature

Raman investigations on $Y_{1-x}Ca_xTiO_3$ are available in the literature [32, 33]. In [32] Raman spectra of different doping levels across x_{MIT} are published. Fig. 3.6 shows low temperature Raman spectra of insulating and metallic samples around x_{MIT} and the spectra for $x = 37\%$ and $x = 41\%$ show, that the Raman spectra are quite distinct between insulating and metallic samples. Since this interesting result is of relevance for this work, it is explicitly shown here. Fig. 3.7 shows furthermore the doping evolution of the Raman spectra at RT in $c(aa)\bar{c}$ geometry, showing that the phonon peaks broaden with doping but the energies do not change significantly. This suggests, that mode assignments on $YTiO_3$ can be transferred to the doped materials.
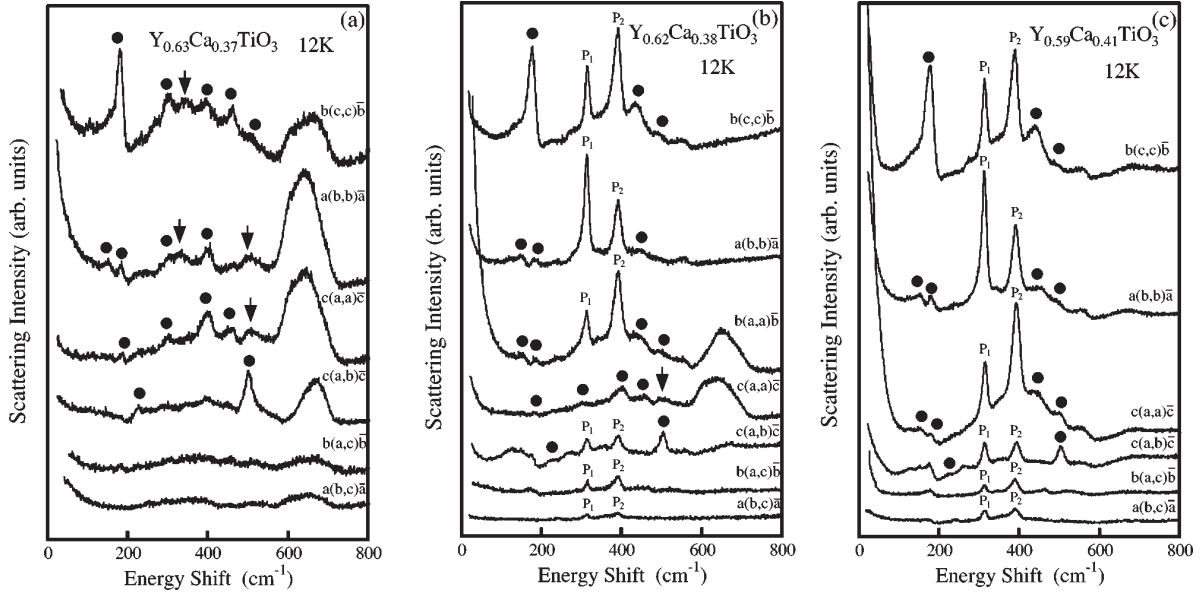
Fig. 3.6: The low temperature Raman spectra of $Y_{1-x}Ca_xTiO_3$ near x_{MIT} [32].
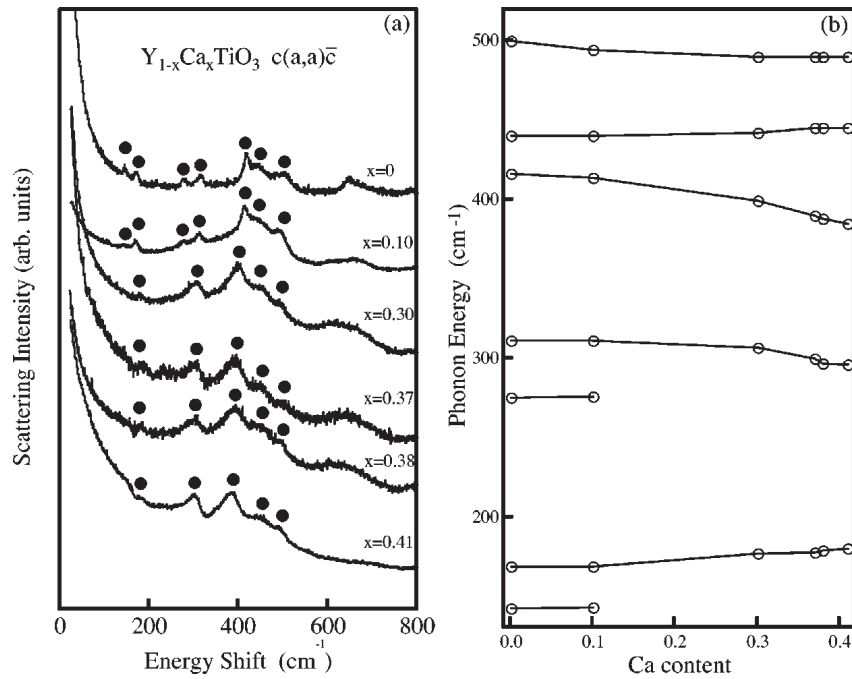
Fig. 3.7: RT Raman spectra of $Y_{1-x}Ca_xTiO_3$ with varying x [32].

4. EXPERIMENTAL RESULTS

In this chapter the measurements conducted on $Y_{.63}Ca_{.37}TiO_3$ and their analysis are presented. The characterization of the material via SQUID susceptibility measurement is presented in sec. 4.1. The results of the optical microscope investigations are shown in sec. 4.2 and the Raman spectroscopy studies are presented in sec. 4.3. Single crystalline pieces of the ACK083 sample grown by A. Komarek [8] are used for the measurements. For the optical microscope and Raman measurements, the samples were oriented via Laue diffraction and the surfaces were mechanically polished.

4.1 Magnetic susceptibility
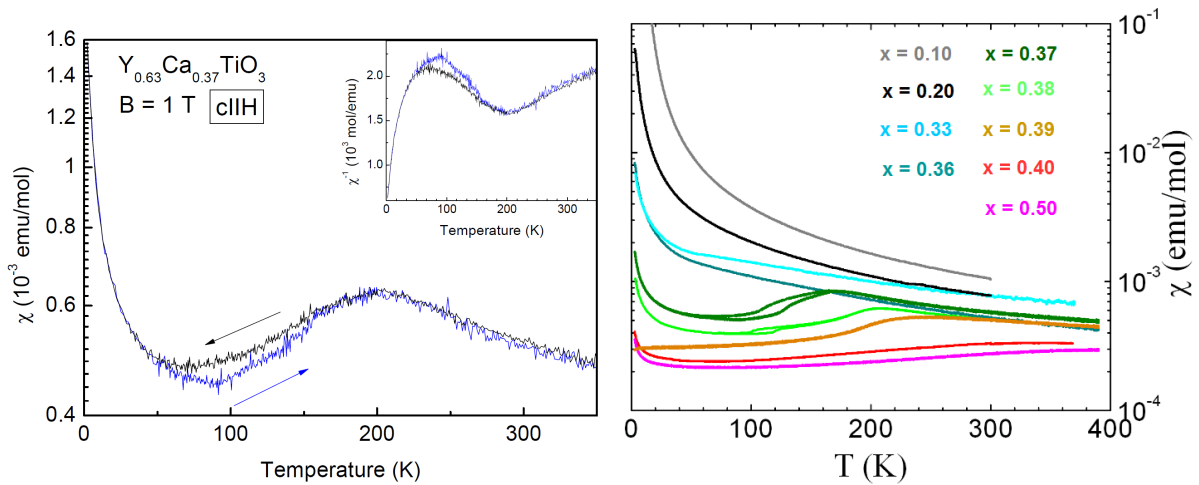
Fig. 4.1: Left: Temperature dependent SQUID-magnetometer measurement of the $Y_{.63}Ca_{.37}TiO_3$ sample. Right: The magnetic susceptibilities of $Y_{1-x}Ca_xTiO_3$ for several x [8], as a reference to compare the χ measurement of this work.

The magnetic susceptibility χ and its temperature dependence was measured by S. Heijligen with a SQUID magnetometer MPMS-XL of the company Quantum Design. The measurement was done with an applied B-field of 1 T parallel to the c-direction and is shown in fig 4.1, left. This measurement serves as a characterization of the used sample, since the magnetic susceptibilities of $Y_{1-x}Ca_xTiO_3$ are well known and are shown for several x in fig. 4.1, right. Comparing

the temperature evolution of the measured χ from fig. 4.1, left, with the $x = 0.37$ magnetic susceptibility in fig. 4.1 as reference, it is seen, that the used sample reproduces the temperature behaviour of the reference quite well. The measured sample has a Curie like behaviour at low temperatures and rises between $\gtrsim 90\,\mathrm{K}$ and $\sim 200\,\mathrm{K}$. Above $\sim 200\,\mathrm{K}$ it decreases again. Between $\sim 58\,\mathrm{K}$ to $\sim 168\,\mathrm{K}$ it exhibits also a hysteresis which reproduces the hysteresis of $x = 0.37$ materials. In [34] it is shown, that χ can be modelled by describing the metallic LTO phase by a sum of Pauli paramagnetic term and Curie law and the insulating LTM phase by a Curie-Weiss law. The measured χ then corresponds to the sum of the susceptibilities of the coexisting phases, weighted by their volume fractions. This behaviour is more directly seen in an inverse χ-plot (fig. 4.1, left, inset), where at low temperatures a roughly linear slope corresponds to the Curie law of the metallic phase and at higher temperatures (above $200\,\mathrm{K}$) the linear slope corresponds to the Curie-Weiss behaviour of the insulating phase. The hysteresis region in between is characterized by the rather strong change of the volume fractions of the coexisting phases.

The agreement in the magnetic susceptibility concludes that the doping level of the used sample is still $x \approx 0.37$. It is therefore suited for more elaborate investigations to study the metal insulator transition and phase separation in $\mathrm{Y}_{1-x}\mathrm{Ca}_x\mathrm{TiO}_3$. The inflection point at $\sim 200\,\mathrm{K}$, which corresponds more to the temperature behaviour of $x = 0.38$ materials could be a hint, that the doping level of the used sample may be slightly bigger than $x = 0.37$.

4.2 Optical microscopy

Polished samples of $\mathrm{Y}_{.63}\mathrm{Ca}_{.37}\mathrm{TiO}_3$ were investigated by conventional optical microscopy in back-reflection geometry, using the Olympus BX51w1 microscope of the Princeton Instruments Trivista Raman spectrometer. Here the sample surface was illuminated by a non-polarized white light source and the reflection of the surface was detected by a CCD camera. The cryostat used for cooling is the same as the one used for the Raman measurements. A microscope objective of 8x magnification and numerical aperture of 0.18 was used to follow the temperature evolution of the reflection of the sample's surfaces. Generally the spatial resolution of the microscope sets a lower limit on the observable domain sizes. Patterns smaller than $\sim 2\,\mathrm{\mu m}$ cannot be resolved any more with the used microscope setup.

In fig. 4.2 the temperature evolution of the reflection from the surface of the $\mathrm{Y}_{.63}\mathrm{Ca}_{.37}\mathrm{TiO}_3$ (001)-sample upon cooling is shown. Starting at room temperature (see fig. 4.2, top left) a slight dark-bright patterned contrast is very weakly discernible[1]. Lowering the temperature, this contrast continuously increases and a pattern of brighter structures on a slightly darker background

---

[1] This is more clearly seen in the electronic version of the thesis.
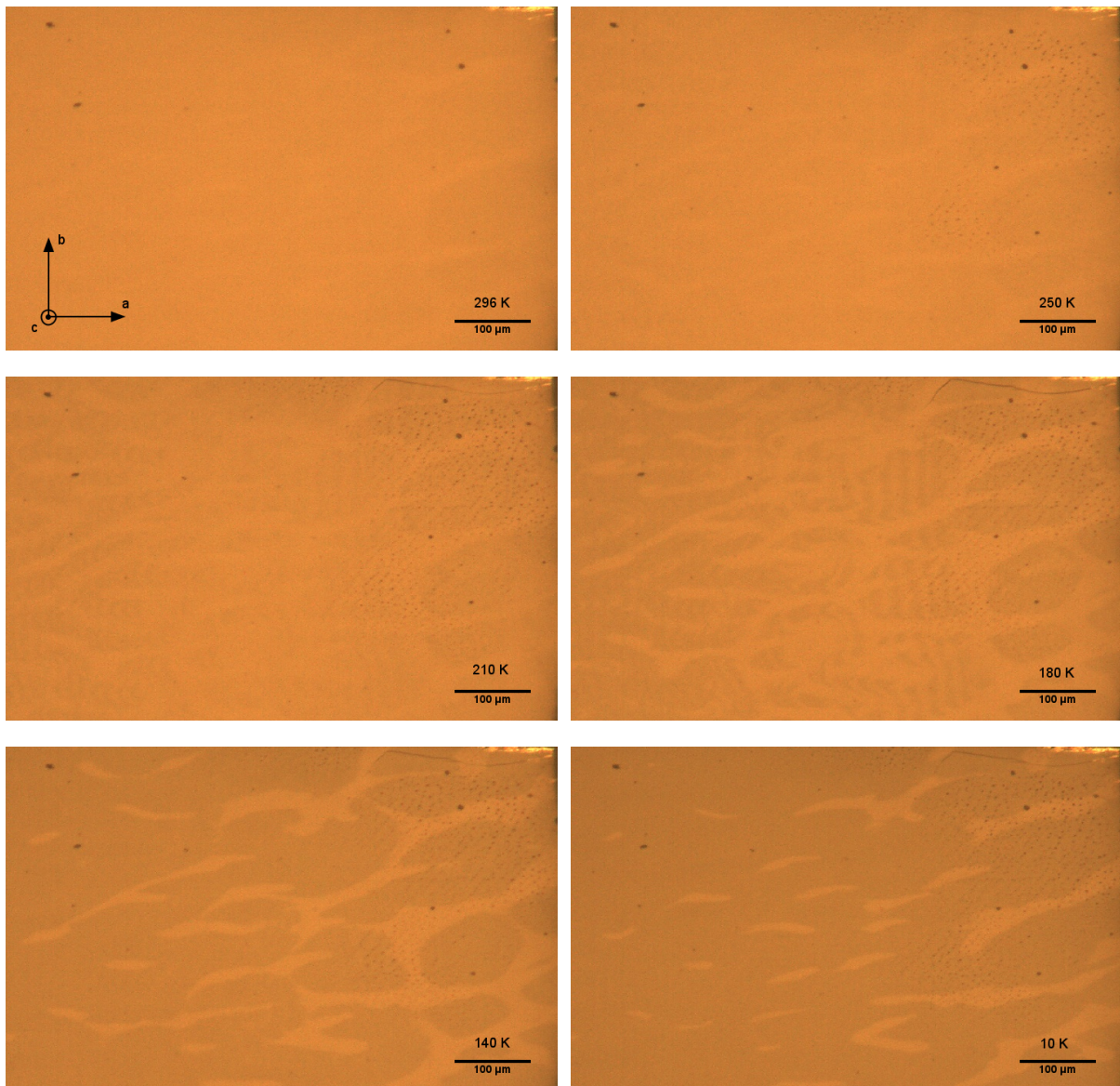
Fig. 4.2: Microscope pictures of the (001)-sample of $Y_{.63}Ca_{.37}TiO_3$, illuminated by white light. The orientation is drawn in the 296 K picture (top, left) and the picture series shows the pattern evolution on the surface upon lowering the temperature.

becomes more clear. As the contrast between brighter and darker areas increases, the darker areas extend on cost of the brighter areas. Towards lower temperatures, the dark areas seem to grow by trend roughly in [100] direction, which is seen in fig. 4.2 comparing the 180 K, 140 K and 10 K pictures. Considering again the pattern indicated at RT, this pattern seems to correspond in large part to the bright pattern visible at lower temperatures like $\sim$ 140 K and lower.

Looking more closely on the pattern formation in the cooling ramp, it looks like around 220 K-210 K (fig. 4.2) bright stripes directed in [010] direction start to form. The width of these stripe like patterns is roughly 20 µm and decreases upon cooling. This decrease goes along with the darker areas dominantly extending in [100] direction, making these stripe like patterns vanish at $\sim$ 140 K.

From the known structural and electronical phase evolution in this material, the observed temperature behaviour suggests the hypothesis, that the darker and brighter areas each correspond to a single domain. Meaning that the dark domain would correspond to the metallic phase and the bright domain to the insulating phase of the material. This hypothesis will be later strengthened by the Raman measurements.
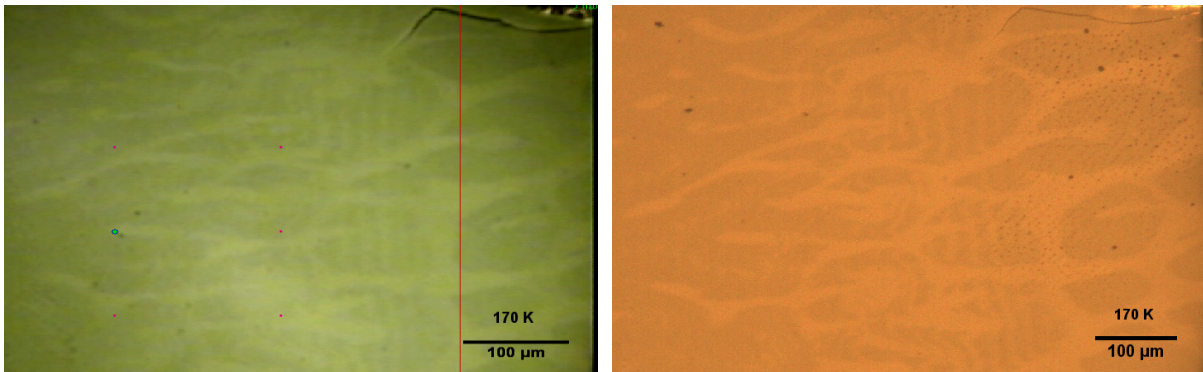
Fig. 4.3: Comparison of microscope pictures at 170 K, left from August 2014, right from February 2015, showing the pinning of the domains.

Temperature cycles show that the patterns are spatially fixed. In fig. 4.3 two pictures recorded six months apart of the (001)-sample are shown, showing that the patterns have not changed. This shows that the domains are pinned. The most likely main reason for this is a spatial chemical inhomogeneity w.r.t. the doping level or oxygen stoichiometry. Near x_{MIT} small deviations in doping level or stoichiometry would shift the material closer to the metallic or insulating side in the phase diagram. Quenched disorder induced by the Ca^{2+} and Y^{3+} configuration thus seems to have an important influence on the phase separation in $Y_{1-x}Ca_xTiO_3$. Spatial chemical inhomogeneity could also explain why the patterns of the (001)-sample are still discernible even at RT.
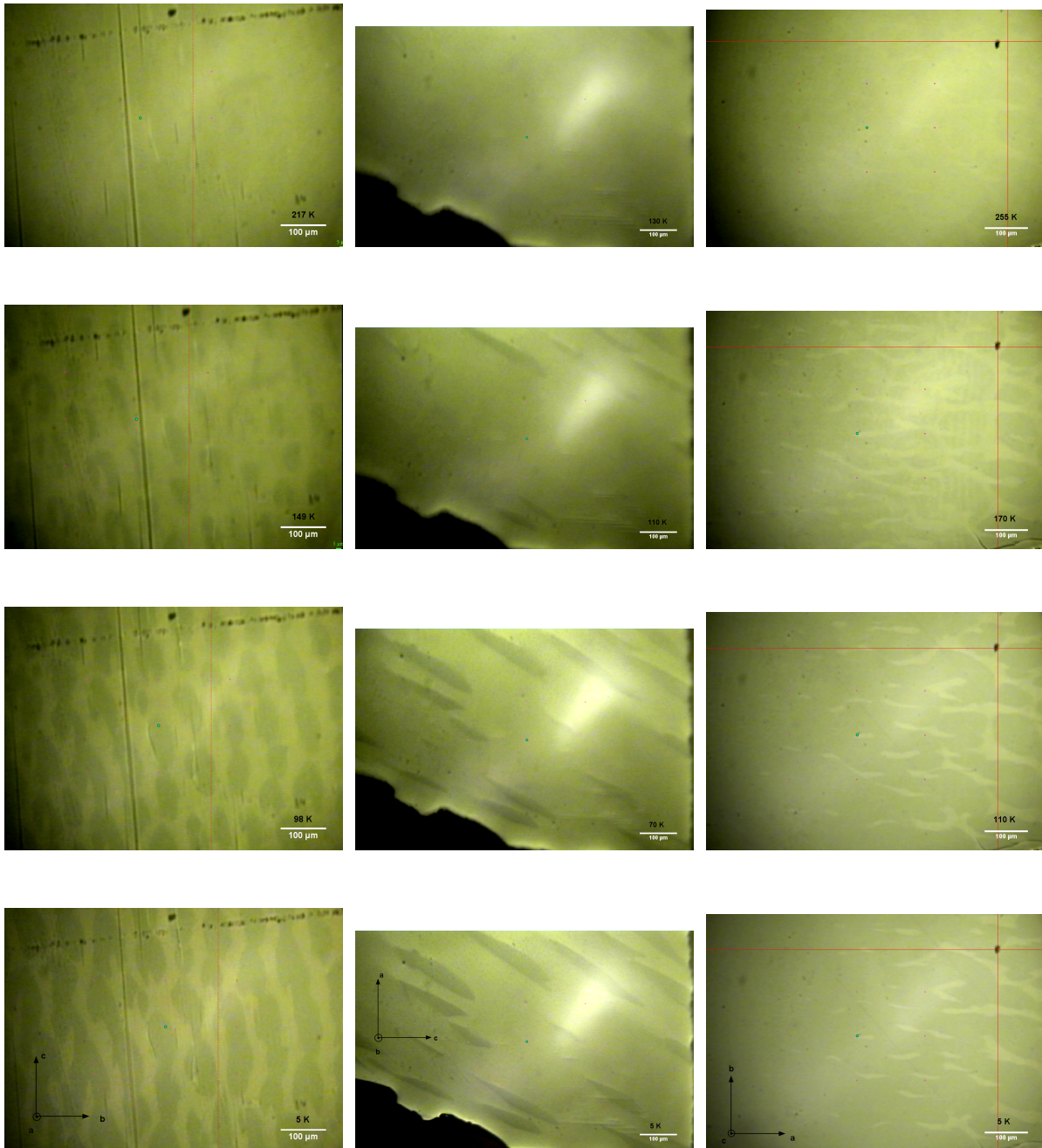
Fig. 4.4: Temperature evolution of the domain patterns of (100)-, (010)- and (001)-sample of Y$_{.63}$Ca$_{.37}$TiO$_3$ from left to right.

In fig. 4.4 the temperature evolution of $Y_{.63}Ca_{.37}TiO_3$ (100), (010) and (001) surfaces are shown. For all three orientations, dark domains increase in weight on cost of bright domains upon cooling and in each case there is a main growth direction of the dark domains. In the (100)-sample the dark domains grow predominantly in [001] direction until the isolated single domains connect and form a percolation network at lowest temperatures. The dark domain patterns in the (010)-sample, appear to grow predominantly in [110] direction, but the isolated single domains do not connect. And as already mentioned, the dark domains in the (001)-sample grow predominantly along the [100] direction and also connect at lower temperatures. Identifying the dark domains with the metallic phase, it appears that on a very large scale percolation phenomena appear, where the [100] and [001] directions would correspond to directions of high conductivity. In contrast, the [010] direction appears to be perpendicular to the metallic percolation directions, meaning that the conductivity would be strongly suppressed in that direction. Such described anisotropy in the resistivity is indeed observed [32] and shown in fig. 4.5, left. This observed domain evolution of the dark domain upon cooling indicates that the insulator-metal transition in the resistivity corresponds to a percolation transition.

It is interesting to note, that the domain patterns of $Y_{1-x}Ca_xTiO_3$ observed by transmission electron microscopy (see fig. 4.5, right, [17]), have similarities with the patterns seen under the optical microscope in this work . Although the length scales of the domains observed by TEM and the domains observed by optical microscopy differ up to roughly three orders of magnitude, the predominant orientations described above and the domain shapes are similar. This could hint to a scaling behaviour of the domain patterns.
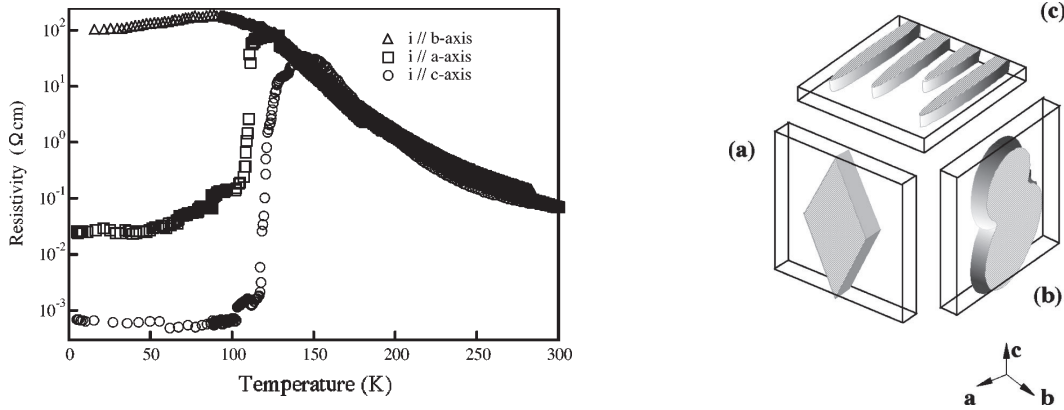
Fig. 4.5: Left: Resistivity measurements of $Y_{.62}Ca_{.38}TiO_3$ along (100), (010) and (001) direction [35]. Right: Domain patterns observed by TEM [17].

Finally the assignment of dark domains belonging to the metallic phase and bright domains being identified with the insulating phase shall be commented. The fact that the metallic phase is identified with the darker domain may appear counter intuitive on first sight. Metals are usually considered to have higher reflectivity due to their free charge carriers. In the Drude

model describing the response of free electrons on an electric field, the Reflectivity R is equal one below the plasma frequency ω_P, which is typically bigger than optical frequencies [36]. Only above ω_P the metal starts to absorb, if there are no interband transitions below ω_P. However the plasma edge of metallic $Y_{1-x}Ca_xTiO_3$ samples is reported to be around $\sim 1\,eV$ on the basis of reflectivity measurements [9], which are shown in fig. 4.6, left. For $x = 0.6$ and 0.8 metallic samples, the plasma edge is readily seen around $1\,eV$, where the reflectivity decreases quite strongly. Magnification of the reflectivity values in the optical frequency range, comparing insulating $x = 0.2$ with metallic $x = 0.4$ and 0.6 samples directly shows that the reflectivity of the insulating sample is slightly higher than that of the metallic samples. An estimation of the plasma frequency ω_P can be also obtained from the electronic specific heat capacity c_V, using the thermodynamic relations of a Fermi liquid [37]. With the relation $c_V = \frac{(\pi k_B)^2}{3}D(E_F)T = \gamma T$ and $D(E_F) = \frac{V}{\pi^2}\frac{m^*}{\hbar^2}(3\pi^2 n)^{1/3}$, ω_P is obtained via its definition $\omega_P^2 = \frac{ne^2}{\epsilon_0 m^*}$, where $D(E_F)$ is the density of states at the Fermi energy E_F of the charge carriers, m^* and n their effective mass and volume densities respectively. Using the γ value for $x = 0.4$ sample from [38], a plasma frequency $\hbar\omega_P = 1.1\,eV$ is obtained. This confirms the assignment of the plasma edge in the reflectivity measurements (fig. 4.6) at around $1\,eV$. Thus the observation in this work, that the metallic phase has a lower reflectivity than the insulating phase is consistent with former experiments.
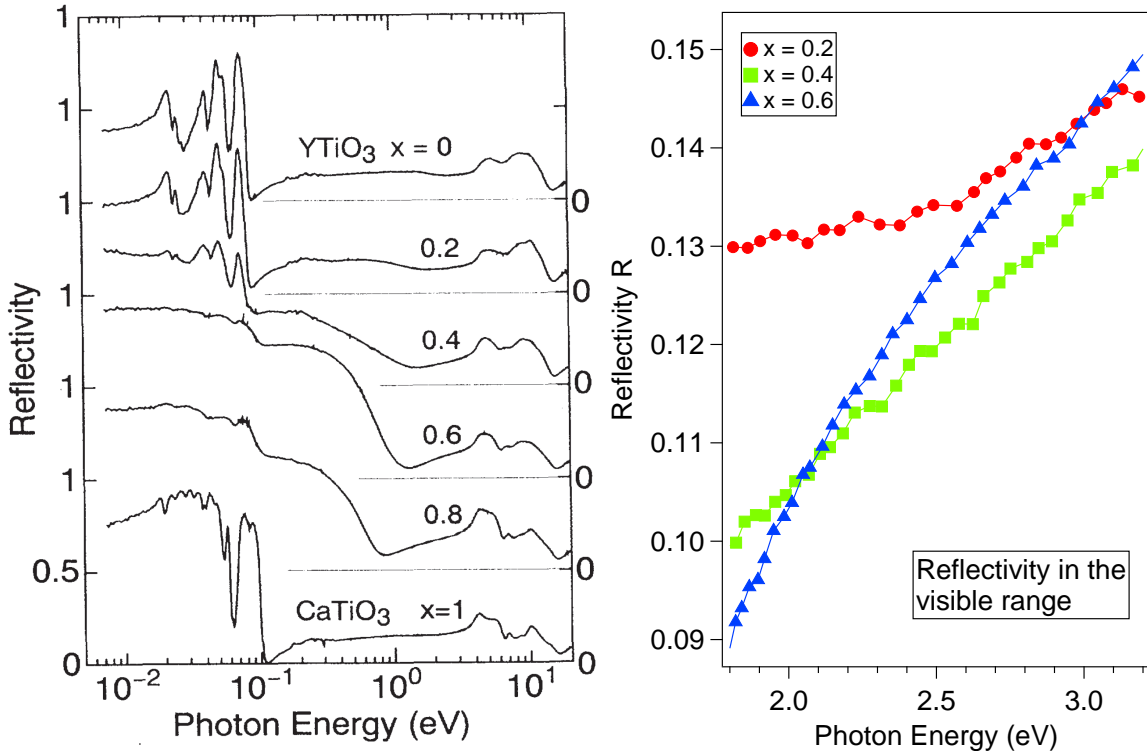
Fig. 4.6: Left: the reflectivity of $Y_{1-x}Ca_xTiO_3$ for several x at RT [9]. Right: Magnification of the reflectivity values in the optical regime for $x = 0.2$, 0.4 and 0.6 samples.

4.3 Raman investigation

The polished (001)-sample used for the optical microscopy studies (sec. 4.2) was also investigated with the micro-Raman setup described in sec. 3.3. As the observed domains under the optical microscope are on the order of ten to hundred micrometer in size at low temperatures (fig. 4.2), it is possible to probe the two domains separately with the used laser spot size of $\sim 30 \, \mu m$. To follow the temperature evolution of the Raman spectra of bright and dark domains, the position of the laser spot was fixed for each domain for all temperatures of a ramp. Note that, since the measurement positions are fixed, the measurements are referred to as bright- and dark-domain-measurements even at high temperatures, although strictly speaking this is not correct any more for the area being a dark domain at low temperatures. For the heating ramp which is in the following discussed and analysed, each spectrum was integrated in total one hour with a laser power of $1.7 \, mW$ at the sample and the polarization geometry was $c(aa)\bar{c}$. Background subtraction (see also sec. 3.3, fig. 3.5) is done in an energy range from $\sim 250 \, cm^{-1}$ to $\sim 800 \, cm^{-1}$. The spectra showing the full energy range are not background corrected.
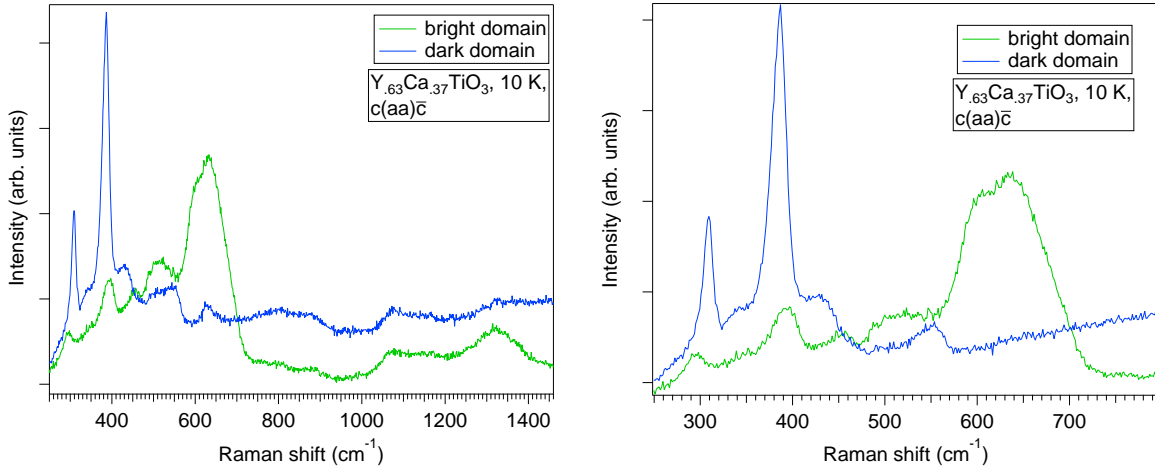
Fig. 4.7: The $c(aa)\bar{c}$ Raman spectra of dark and bright domains at $10 \, K$ of $Y_{.63}Ca_{.37}TiO_3$. Left: Full energy range without background subtraction. Right $\sim 250 \, cm^{-1}$ to $\sim 800 \, cm^{-1}$ spectra which are background corrected.

Fig. 4.7 shows the low temperature Raman spectra probed from bright and dark domain each. The spectra from both domains are really distinct. In the dark domain spectrum, the $\sim 300 \, cm^{-1}$ and $\sim 400 \, cm^{-1}$ peaks are narrower than those in the bright domain spectrum. Also the peak positions differ which is shown in fig. 4.9. In the broad energy spectrum (fig. 4.7, left) an enhancement of the background scattering in the dark domain spectrum above $700 \, cm^{-1}$ is visible. At $\sim 630 \, cm^{-1}$ a broad feature of high intensity is seen in the bright domain spectrum, which is completely suppressed in the dark domain spectrum (see fig. 4.7, right). Such a clear difference in the Raman spectra strongly suggests, that the bright domains and the dark domains

belong to two different phases. Comparing the spectra with the Raman data in literature [32] shown in fig. 3.6, it is seen, that the low-T bright domain spectrum and the $x = 0.37$ low-T spectrum correspond to each other. In [32] it is stated, that *"the metallic behaviour has not been observed even at* $12\,K$*"* for their $x = 0.37$ sample, meaning that their Raman spectrum is that of an insulating sample. The low-T dark domain spectrum in contrast agrees with the $x = 0.41$ low-T spectrum from [32], which is a metallic sample. The comparison with the literature thus suggests, that the low-T dark domain spectrum corresponds to the metallic phase Raman spectra and the low-T bright domain spectrum corresponds to the insulating phase Raman spectra. This is in agreement with the observations and conclusions from the optical microscope measurements in this work (sec. 4.2). Therefore the classification that the dark domains belong to the metallic phase and the bright domains belong to the insulating phase is further strengthened by the Raman measurements.
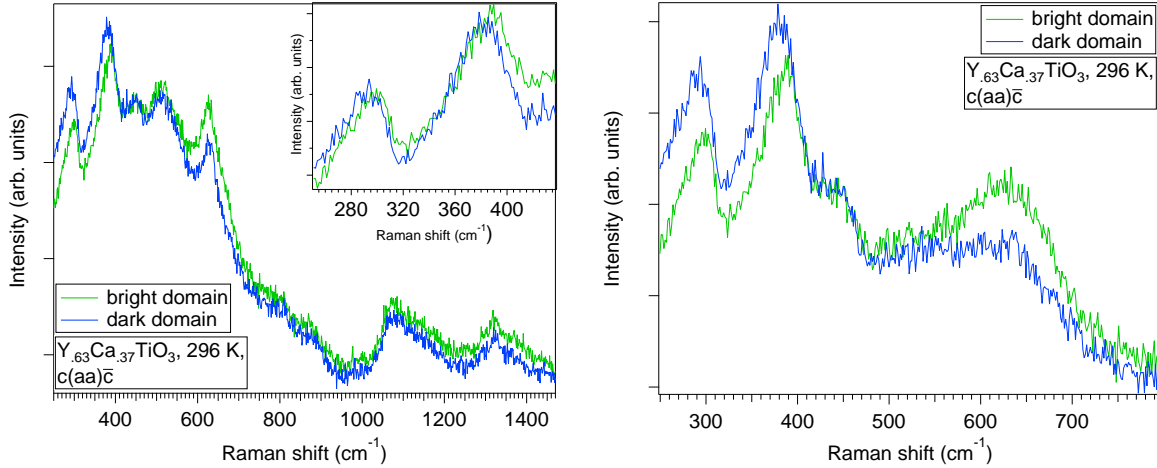
Fig. 4.8: The $c(aa)\bar{c}$ RT Raman spectra of dark and bright domains of $Y_{.63}Ca_{.37}TiO_3$. Left: Full energy range without background subtraction. The inset shows the $\sim 300\,cm^{-1}$ and $\sim 400\,cm^{-1}$ peaks, to indicate the slight energy shifts (green curve offset for visualisation purpose). Right: $\sim 250\,cm^{-1}$ to $\sim 800\,cm^{-1}$ spectra which are background corrected.

As described in sec. 4.2, contrast between the bright and dark areas is still recognizable up to RT, which is also manifested in slight differences between the Raman spectra of bright and dark domains at RT. The $\sim 300\,cm^{-1}$ and $\sim 400\,cm^{-1}$ peaks are shifted in energy between both domains even at RT, as shown in the inset of fig. 4.8, left, and fig. 4.9. Also peak weights differ, which is especially the case for the $\sim 630\,cm^{-1}$ structure (see fig. 4.8, right). These differences in energy and weight of peaks in the Raman spectra even at RT further strengthens the hypothesis suggested in sec.4.2, that the chemical composition like doping level, oxygen stoichiometry or defect densities is spatially inhomogeneous in this material.
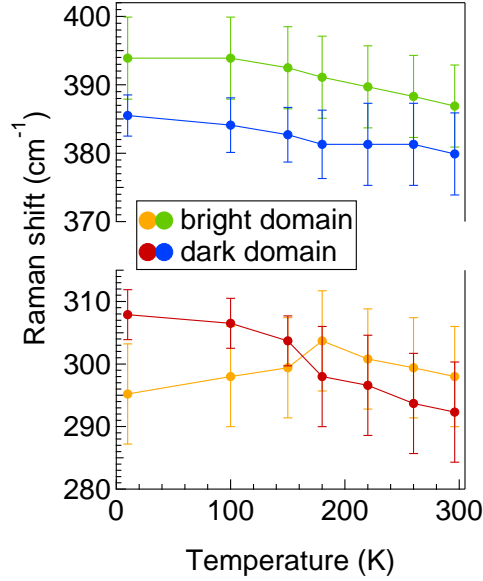
Fig. 4.9: Energies of the peak maxima of the $\sim 300\,\mathrm{cm}^{-1}$ and $\sim 400\,\mathrm{cm}^{-1}$ peaks.

More specific information is obtained from phonon mode assignments to the Raman spectra. The normal mode decomposition for the Raman active modes reads (see sec. 3.1): $7A_g + 7B_{1g} + 5B_{2g} + 5B_{3g}$ in $Pbnm$. The A_g-modes can be probed in parallel polarization and the B_{ig}-modes are observable in cross-polarized geometry $(ab),(ac),(bc)$ for $i = 1,2,3$. The phase transition from orthorhombic $Pbnm$ to monoclinic $P2_1/n$ phase leads only to a redistribution of orthorhombic B_g-modes to monoclinic A_g symmetry. In $Pbnm$ this means that the orthorhombic B_{2g}-modes become A_g-modes in the monoclinic phase, if the tilting angle is the β-angle. Orthorhombic $Pbnm$ and monoclinic $P2_1/n$ phases are therefore expected to be distinguishable in the Raman spectra: B_{2g}-modes which are visible in the orthorhombic phase only in cross-polarized geometry, can become visible in the monoclinic phase in parallel polarized geometry.

Explicit assignment of the observed peaks to specific lattice vibrations is taken from isostructural $YMnO_3$ [39]. As the Ti^{3+}/Mn^{3+} ions do not participate in the Raman active modes, there is no shift in the mode energies due to their different masses. However the force constants between Ti-O bonds and Mn-O bonds may differ and lead to differences in the phonon energies. Comparison of the mode energies between $YMnO_3$ and $YTiO_3$ [41] shows nevertheless a good agreement as is shown in the appendix, sec. B, tab. B.1, listing all Raman active modes. Considering the influence of doping, fig. 3.7 shows, that the frequencies of $Y_{1-x}Ca_xTiO_3$ remain similar to the frequencies of the undoped parent compound in doping ranges of interest here. For a direct comparison, the mode energies of $Y_{.63}Ca_{.37}TiO_3$ obtained from the fits in this work (see below) are also listed in appendix, sec. B, tab. B.1. The similarity of the mode energies confirm the trend that the energies of the doped compounds are still comparable to the undoped compound. This suggests that the mode assignments from [39] can be directly transferred to the investigated material here. The modes which are of interest in the following are shown in fig. 4.10.
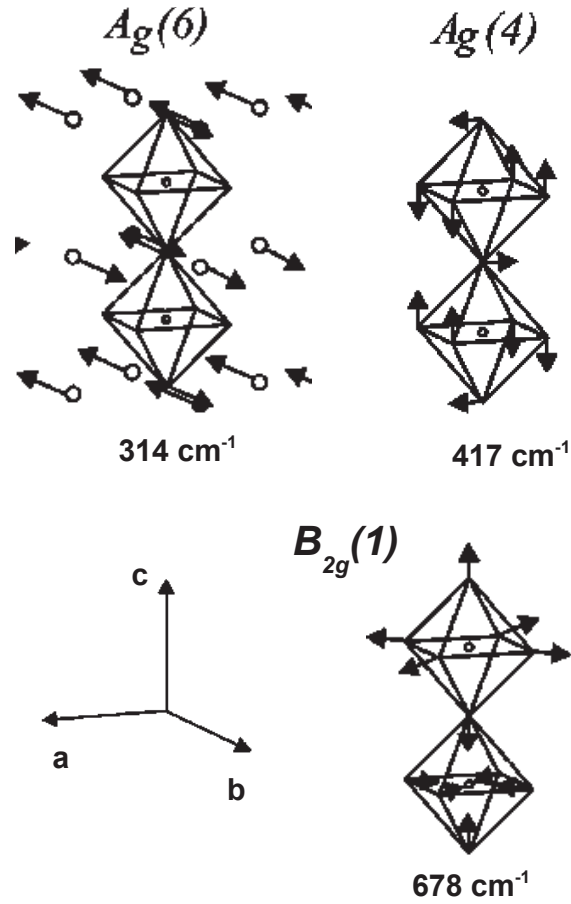
Fig. 4.10: Selection of phonon modes from *Pbnm* space group [40]. What is seen are the TiO_6 octahedra and the arrows indicate the vibrational pattern. In the $A_g(6)$ mode, the Y (or Ca) ions also participate in the vibration, in contrast to the other modes listed here, where they are just omitted. Top row shows the $\sim 300\,cm^{-1}$ and $\sim 400\,cm^{-1}$ modes and bottom row shows the breathing mode. The frequencies refer to assignments from low-T $YTiO_3$ measurements [41].

To quantify the temperature evolution of the Raman spectra, the spectra are fitted in the energy range from $250\,cm^{-1}$ to $800\,cm^{-1}$. As it is seen in tab. B.1 (App. B), the phonon energies all lie between $142\,cm^{-1}$ and $678\,cm^{-1}$, so it is reasonable to assume that the Raman spectra in this energy range consist mainly of phonons. It is therefore modelled by a sum of phonon lineshapes (eq. 3.10), which is described in more detail in sec. 3.2. The fits are initialised by choosing a minimal set of oscillators in the 10 K spectra, since there the spectral features are most sharp. In fig. 4.11 the chosen oscillators for the dark and bright domain spectra with the corresponding fits are shown. With the chosen set of oscillators at 10 K, the fitting parameters obtained there are used as initializations for the next temperature spectrum of the ramp *etc.* In appendix, sec. C the fit results for all temperatures are listed.
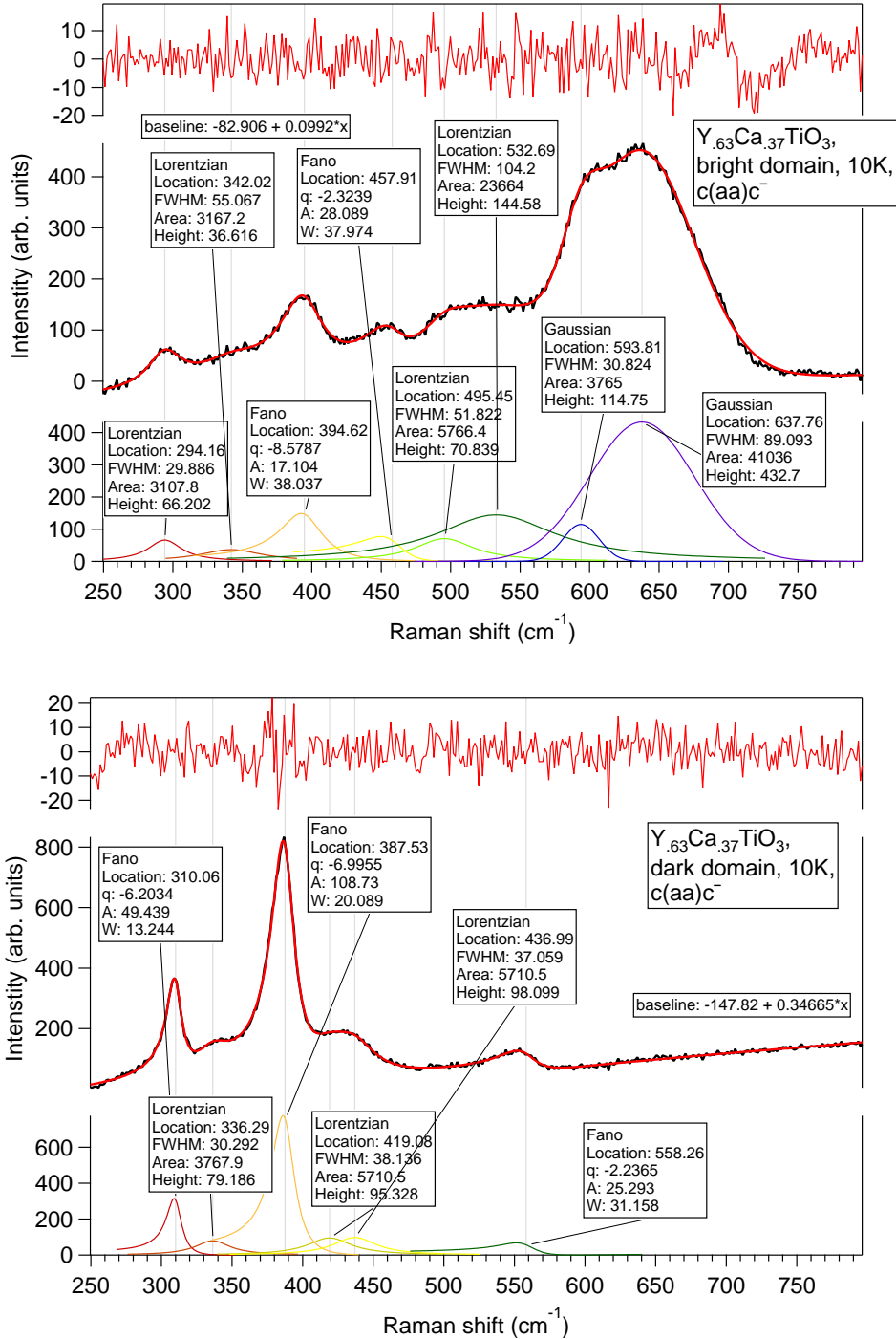
Fig. 4.11: The 10 K fits of the $c(aa)\bar{c}$ Raman spectra, showing the chosen oscillators for the bright domain spectrum (top) and dark domain spectrum (bottom) respectively. Above the spectra the residuals of the fits are shown and below the spectra the explicit chosen oscillators are plotted.

To have an overview over the temperature behaviour of bright and dark domain Raman spectra, the temperature heating ramp is shown in fig. 4.12. There the bright domain spectra are offset to match at $\sim 760\,\mathrm{cm}^{-1}$ and the dark domain spectra are offset to match at $\sim 480\,\mathrm{cm}^{-1}$, to visualize the temperature evolution of the modes better. In the following, the results and discussion of the fits are divided up w.r.t. bright and dark domain measurements respectively.
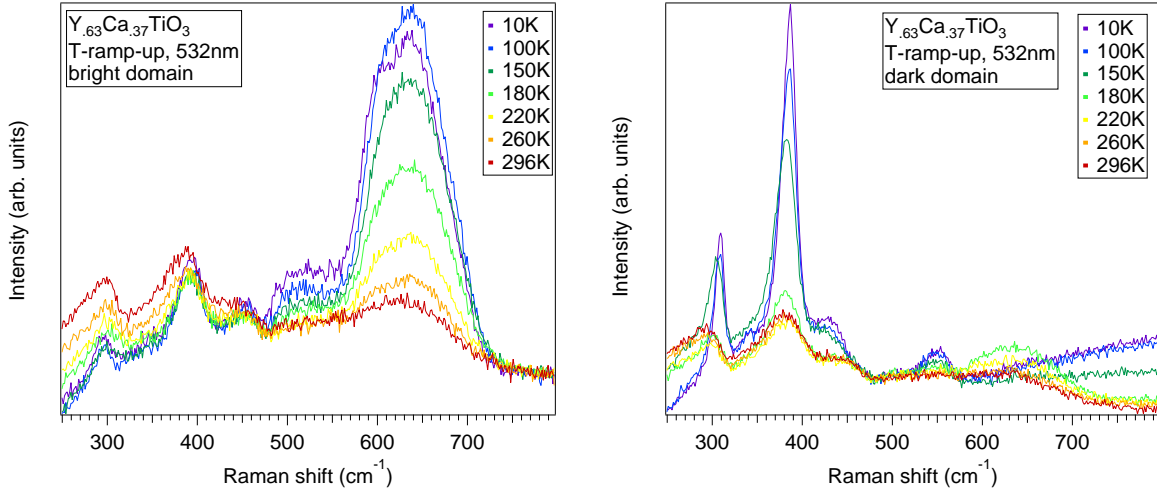
Fig. 4.12: The temperature heating ramp of $c(aa)\bar{c}$ Raman spectra, where the laser is spatially fixed at a specific point. Left: The bright domain spectra. Right: The dark domain spectra.

First the bright domain spectra are considered and as the results so far suggest, the bright domains are associated with the insulating phase. The LTM phase is reported to undergo a structural phase transition in a temperature range between $170\,\mathrm{K}$-$230\,\mathrm{K}$[5, 8, 17]. It is however not possible to determine a clear structural transition in the bright domain Raman spectra (fig. 4.12, left), as the temperature behaviour of the peaks differ.

Of particular interest is the broad feature at $\sim 630\,\mathrm{cm}^{-1}$. The polarization geometry and the calculated frequencies (tab. B.1, app. B) suggest that the feature consists in part of the $B_{2g}(1)$ breathing mode , which becomes active in parallel polarization in the monoclinic phase. Due to twinning [8] the broad feature most likely consists also of the $B_{3g}(1)$ mode, which is lower in energy than the breathing mode. As is seen in fig. 4.11 and 4.12, these peaks do not appear in the low temperature dark domain spectra at all, thus being inherent to the LTM phase. To fit the $\sim 630\,\mathrm{cm}^{-1}$ feature, gaussian lineshapes give better results than Lorentzians, indicating that both modes are sensitive to the randomness of the local environment induced by the Ca^{2+}/Y^{3+} disorder. The peak weight of the $B_{2g}(1)$ breathing mode obtained from the fits, shows a strong temperature behaviour, which is shown in fig. 4.13. Upon decreasing temperature, the peak weight of the breathing mode strongly increases and reaches saturation around $100\,\mathrm{K}$. Saturation towards lower temperatures is reported also in the static G-type distortion

pattern associated with the charge and orbital order of the LTM phase [7, 8]. The vibrational pattern of the breathing mode corresponds to out of phase stretching of the TiO_6 octahedra, that is an alternating contraction and expansion of neighbouring octahedra, which is shown in fig. 4.10. It thus actually corresponds to the static G-type distortion pattern (see fig. 2.2). This similarity in temperature dependence suggests, that the weight of the breathing mode in the Raman spectrum is sensitive to the strength of the distortion. Furthermore saturation exists also in the unit cell parameters when considering the differences between LTO and LTM phases, which increase and saturate towards lower temperatures [5, 8]. A direct comparison of the weight of the breathing mode and the unit cell volume differences of both phases denoted by ΔV is shown in fig. 4.13, right. For ΔV the data of the $x = 38\%$ sample are used [8] and the log-log plot of the normalized quantities indicates that they are related, yielding a relation of the form $A \propto \Delta V^n$ with $n \approx 2$, if A denotes the peak weight of the breathing mode. As the unit cell volumes of LTO and LTM phases differ, strain plays an important role in the phase separated state [17]. Interpreting ΔV as a measure of strain induced due to the phase separation, a connection between this strain and the G-type distortion is suggested. To check on this connection between strain and distortion, the peak weight of the breathing mode from $Lu_{.56}Ca_{.44}TiO_3$ $c(aa)\overline{c}$ Raman measurements (app. A, fig. A.1) are also plotted into the graph of fig. 4.13, left. $Lu_{.56}Ca_{.44}TiO_3$ (LCTO) is completely insulating (see fig. 2.3) and correspondingly does not phase separate. It is seen, that the temperature dependence of the peak weight of LCTO is much weaker compared to phase separating $Y_{.63}Ca_{.37}TiO_3$ material. This indicates, that the strain induced by the phase separation has an influence on the distortion. It is conjectured that due to the similarities in temperature behaviour, strain induced in the phase separated state in $Y_{1-x}Ca_xTiO_3$ is accommodated by enhancing the G-type distortion in the LTM phase. At first sight this conjecture may appear to be counteractive to the fact that the peak weight of LCTO remains high up to RT. Considering the possibility of charge ordering, it is however expected that the G-type distortion and the associated charge ordering is stabilized with increasing x [8], which could account for the remaining high distortion up to RT. A possibility to check the conjecture *e.g.* would be to measure the peak weight in other phase separating $Re_{1-x}Ca_xTiO_3$ samples and compare it to the ΔVs. TEM measurements [17] are also in agreement with the interpretation of G-type distortion being stabilized by the phase separated state. Whereas the LTO phase is observed to be highly strained, the LTM phase is observed to accommodate the strain in such a way, that the symmetry of the LTM phase is maintained. Note the fact, that the peak weight of the used sample is apparently comparable to the data of $x = 38\%$ doping data (fig. 4.13, right) agrees with the results of the susceptibility measurement, which suggest, that the doping level is slightly higher than $x = 37\%$.

Considering in the following the dark domain Raman spectra, which are associated with the spectra of the metallic phase at low temperatures, a significant change between the $150\,\text{K}$ and $180\,\text{K}$ spectra is seen. This is directly visible in the temperature ramp fig. 4.12, right. As seen in
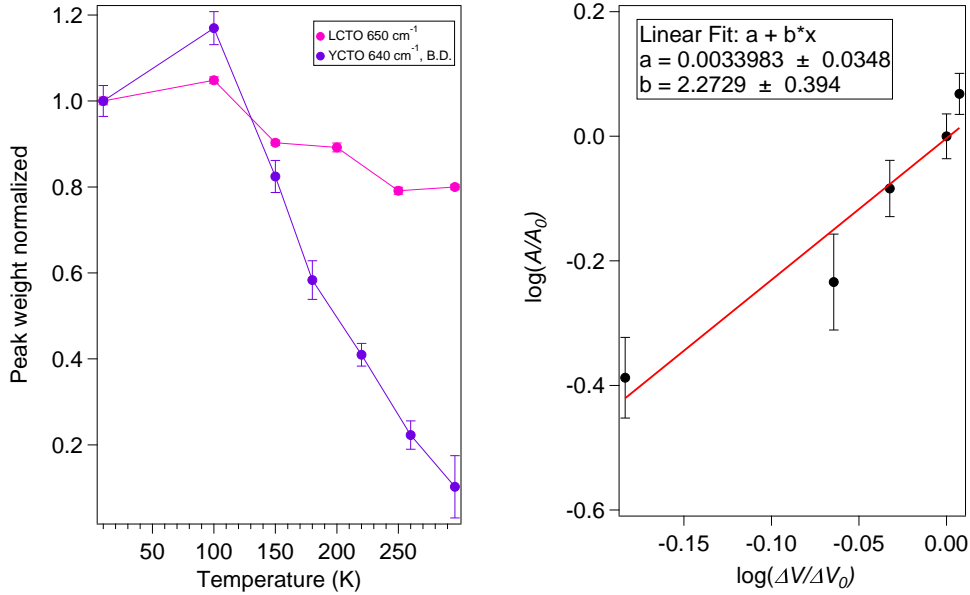
Fig. 4.13: Fitting result of the $630\,\mathrm{cm}^{-1}$ feature of the bright domain Raman spectra. The quantities are normalised to their lowest temperature values respectively. Left: peak weight of the Gaussian corresponding to $B_{2g}(1)$ ($640\,\mathrm{cm}^{-1}$) mode in $\mathrm{Y}_{.63}\mathrm{Ca}_{.37}\mathrm{TiO}_3$ (YCTO, purple). The pink curve furthermore shows the temperature dependence of the breathing mode peak weight from $\mathrm{Lu}_{.56}\mathrm{Ca}_{.44}\mathrm{TiO}_3$ Raman spectra (LCTO). Right: Log-log plot of the peak weight A of the $640\,\mathrm{cm}^{-1}$ mode obtained from the fits and ΔV for $x = 38\%$ doping level [8]. Both quantities are each normalised to their lowest T-value A_0 and ΔV_0.

the optical microscope pictures (fig. 4.2), bright stripes have formed at $180\,\mathrm{K}$ in former dark domains. Thus with the laserfocus of $\sim 30\,\mu\mathrm{m}$ in diameter and stripe widths of $\sim 20\,\mu\mathrm{m}$, the $180\,\mathrm{K}$ spectrum is already a superposition of signal from both bright and dark stripes. This is especially apparent by the appearance of the characteristic feature of the LTM phase at $\sim 630\,\mathrm{cm}^{-1}$ in the $180\,\mathrm{K}$ spectrum, being not visible at all at $150\,\mathrm{K}$ (see fig. 4.14, top). Furthermore a sharp transition is also seen in the linewidths of the $\sim 300\,\mathrm{cm}^{-1}$ $A_g(6)$ and $\sim 400\,\mathrm{cm}^{-1}$ $A_g(4)$ modes (fig. 4.14, bottom), where the linewidths are smaller in the LTO-phase than in the LTM-phase. Thus upon heating, the appearance of the bright domain leads to quite sharp transitions in the Raman spectra between $150\,\mathrm{K}$ and $180\,\mathrm{K}$, since the Raman spectra of metallic and insulating phases are distinct.

Considering the $A_g(6)$ and $A_g(4)$ modes which are the most striking features in the dark domain Raman spectra, it is noted that not all parameters change abruptly between $150\,\mathrm{K}$ and $180\,\mathrm{K}$. Both modes required a description by an asymmetric lineshape in the fits, which is modelled using a Fano line. As described in sec. 3.1 the Fano line arises from a coupling of a sharp line to a continuum of excitations, suggesting a coupling of these modes to the charge carriers in the metallic phase. The fit results of the q-parameters are shown in fig. 4.15 and it is seen that the absolute value of the q-parameters decrease more smoothly upon heating from $10\,\mathrm{K}$ to $180\,\mathrm{K}$ with a corresponding increase of the asymmetry of the lines. In eq. 3.9 it is seen, that this decrease of

$|q|$ can in principle be caused by an increase of the coupling strength V between the phonons and the charge carriers. But also an increase in the density of states ρ of the charge carriers or an increased Raman response T_e of the charge carrier excitations compared to the phonon Raman response T_p would lead to an decrease of $|q|$. At this stage it is not possible to determine the main cause of the enhanced asymmetry of the $A_g(6)$ and $A_g(4)$ modes. A possible increase of the electron phonon coupling could be elaborated further via pump probe measurements of the metallic phase. Looking at the decay rate of the hot electrons generated by the pump pulse, a possible enhanced electron phonon coupling with increasing temperature could be probed with this spectroscopic technique.

In the context of the behaviour of the $A_g(6)$ and $A_g(4)$ modes, it is noted, that similarities are reported in $La_{0.65}Ca_{0.35}MnO_3$ [42]. This material undergoes a phase transition from a paramagnetic insulating to a ferromagnetic metallic state upon cooling. Along with this phase transition an abrupt decrease in linewidth of a Raman mode is observed around T_c. To explain this behaviour a theoretical model taking into account double exchange mechanism of the charge carriers and their coupling to a phonon mode is considered [43]. Furthermore screening of the phonons due to electrons are taken into account. This leads to the result, that with increasing bandwidth, the phonon damping constant decreases. The decrease in linewidth of the observed mode in the Raman spectrum is thus attributed to the bandwidth change of the charge carriers, which is increased upon the insulator to metal transition.
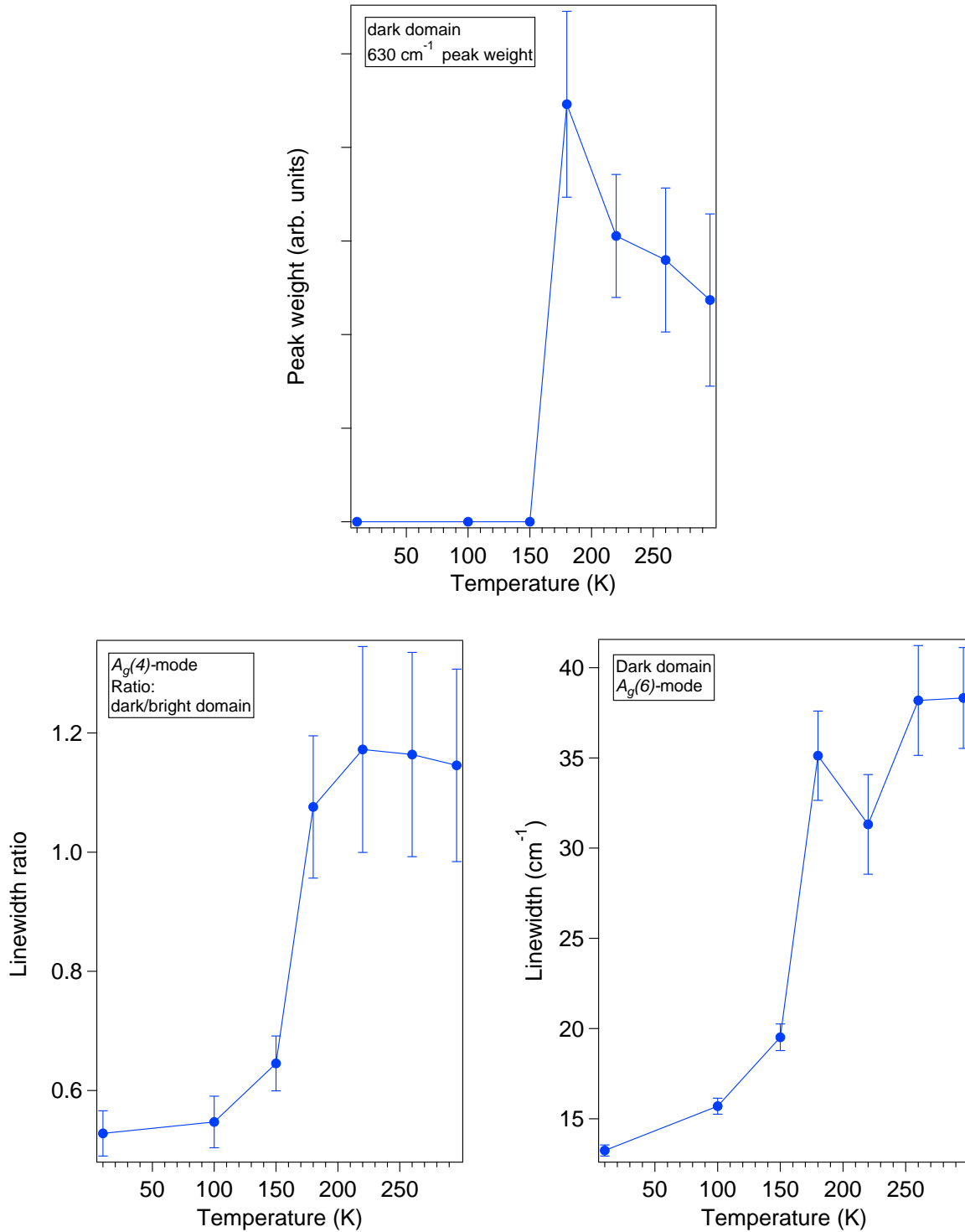
Fig. 4.14: Parameters which show a sharp transition between $150\,\mathrm{K}$-$180\,\mathrm{K}$ in the dark domain spectrum. Top: the peak weight of the $\sim 630\,\mathrm{cm}^{-1}$-feature. Bottom-left: Linewidth ratio dark domain over bright domain of the $A_g(6)$ ($\sim 300\,\mathrm{cm}^{-1}$) mode. Bottom-right: Linewidth of the $A_g(4)$ ($\sim 400\,\mathrm{cm}^{-1}$) mode.
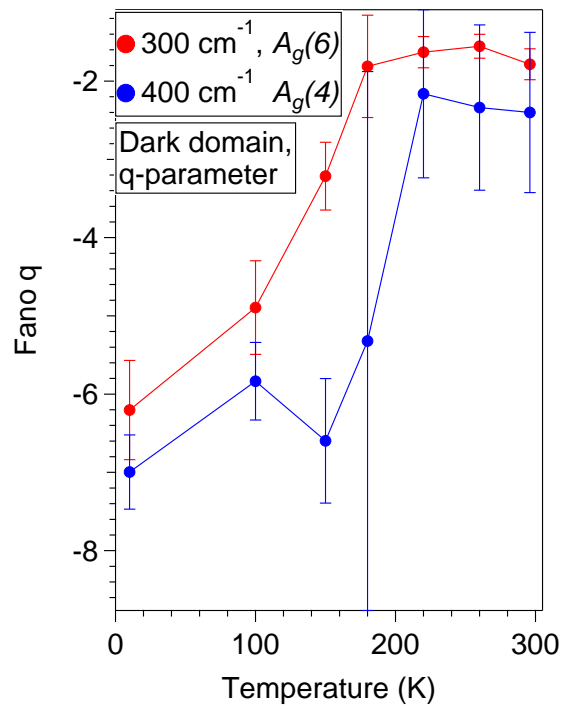
Fig. 4.15: The temperature evolution of the Fano q-parameter of the $A_g(6)$ ($\sim 300\,\text{cm}^{-1}$) and $A_g(4)$ ($\sim 400\,\text{cm}^{-1}$) modes obtained from the fits.

5. CONCLUSION AND OUTLOOK

In this work single crystalline $Y_{.63}Ca_{.37}TiO_3$ is investigated which exhibits a metal to insulator transition with increasing temperature. The sample is first characterised by magnetic susceptibility measurement to verify the doping level of the used sample by comparison with the literature. Using optical microscopy of 8x magnification and spatial resolution of $\sim 2\,\mu m$ it turns out, that it is possible to directly visualise coexistence of bright and dark domains in this material. The observed domain sizes are on the order of few to one hundred micrometer and the temperature evolution exhibits percolation of the domains. By comparison with the known structural and electronic temperature evolution, identification of dark domains with the LTO-metallic phase and bright domains with the LTM- or HTO-insulating phase is suggested. The domain patterns and the growth direction of the domains with varying temperature explains the anisotropy observed in the resistivity [32]. Thus the microscope pictures confirm the hypothesis, that the T-driven MIT is a percolation transition [6].

Using a micro-Raman setup it is possible to probe dark and bright domains separately, exhibiting distinct Raman spectra. The low temperature dark domain spectra and bright domain spectra obtained in this work correspond to Raman spectra of metallic and insulating $Y_{1-x}Ca_xTiO_3$ samples respectively [32], strengthen the assignment made on the domains seen under the microscope.

Raman spectroscopy and optical microscopy exhibit slight differences in phonon energies and contrast between bright and dark domains even at RT. Furthermore the domains are observed to be spatially pinned. This indicates that the material used is spatially chemically inhomogeneous, suggesting that quenched disorder effects contribute to the phase separated state in this material. As the material is near x_{MIT}, it is possible that the chemical inhomogeneity spatially shifts the material away from or closer to the metallic side in the phase diagram, which could be a reason for the huge domain sizes observed in this material. An explicit spatial probing of the chemical composition would be thus of interest. A possible method to do this is micro XPS. It is interesting to note that observations by TEM exhibit similar domain patterns, which are however up to almost three orders of magnitude smaller (hundreds of nanometers) [17]. This might indicate a scaling behaviour of the domains and could be interesting to be elucidated further as it could provide more information on the phase separated state.

In the context of the bright domain Raman spectra a possible influence of strain to the phase separated state is discussed. The breathing mode exhibiting strong temperature dependence with a saturation behaviour in its spectral weight with decreasing temperature, is suggested to

be sensitive to the G-type distortion of the LTM phase. Furthermore a saturation behaviour of the strain induced by the phase separation is suggested, inferred from the different unit cell volumes of coexisting LTO and LTM phases [8]. By comparison with the Raman spectra of non phase separating $Lu_{.56}Ca_{.44}TiO_3$ it is conjectured, that strain induced by phase separation is accommodated by enhancing the G-type distortion and associated charge order of the LTM phase. This suggests that the phase separated state itself influences the electronic properties at least of the LTM phase due to its induced strain. It would be therefore interesting to check on this conjecture more, by comparing *e.g.* the temperature evolution of the spectral weights of the breathing mode in other phase separating $Re_{1-x}Ca_xTiO_3$, comparing it to the lattice parameters. Using thin films grown on substrates could elucidate the effects of strain and phase separation on the single phases in this system in more detail.

The Raman spectra of the dark domains exhibit quite sharp transitions between $150\,K$ and $180\,K$ due to the appearance of bright domains. Besides the appearance of the breathing mode, which is characteristic of the LTM phase, the linewidths of the $A_g(6)$ and $A_g(4)$ modes significantly broaden. However the asymmetric lineshape of both modes modelled by a Fano lineshape exhibit a rather smooth temperature evolution of the q-parameter. The origin of the decrease of $|q|$ with increasing temperature can not be determined at this stage. A possible enhanced electron phonon coupling could be attempted to be extracted from pump probe measurements.

In the end it is noted that the assignment of metallic and insulating phases could be made clear by probing the electron DOS at the Fermi edge in both domains by PES. Such measurements are already performed by T. Koethe and R. German at the Elettra Synchrotron in Trieste and confirm the observations of this work. Spatially resolved probing of the spectral weight at the Fermi edge exhibits stripe like domains of similar sizes as seen under the microscope. The domain patterns here correspond to weight at the Fermi edge or no weight, thus exhibiting coexisting domains of metallic and insulating phases.

APPENDIX

A. RAMAN DATA OF LCTO

In fig. A.1 the temperature series of $c(aa)\bar{c}$ Raman spectra of $\mathrm{Lu}_{.56}\mathrm{Ca}_{.44}\mathrm{TiO}_3$ is shown, which exhibits also a pronounced enhancement of the breathing mode at $\sim 650\,\mathrm{cm}^{-1}$.
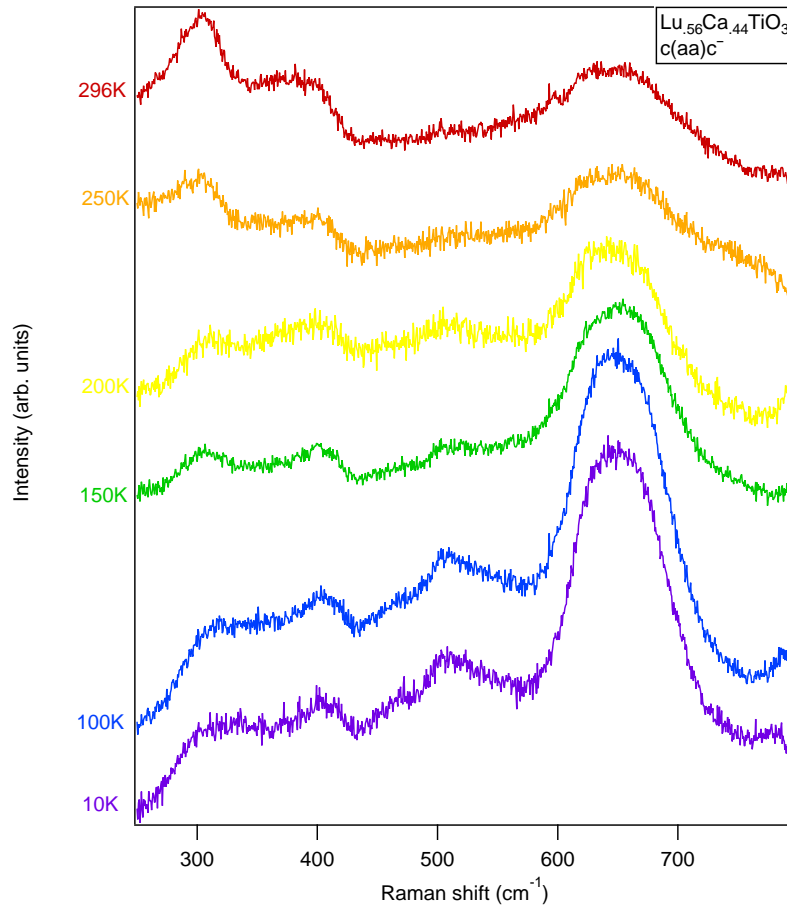
Fig. A.1: The $c(aa)\bar{c}$ Raman spectra of $\mathrm{Lu}_{.56}\mathrm{Ca}_{.44}\mathrm{TiO}_3$ upon heating using a $532\,\mathrm{nm}$ laser line.

B. MODE ASSIGNMENT

In tab. B.1 the Raman active mode energies of isostructural $YMnO_3$ [39] and $YTiO_3$ [41] are listed, showing that the mode assignment in $YMnO_3$ is transferable to $YTiO_3$. Energies in wavenumbers cm^{-1}. The Raman energies of $Y_{.63}Ca_{.37}TiO_3$ obtained from the fits of the $c(aa)\bar{c}$ bright domain measurements at $10\,K$ are also listed. B_{2g} and B_{3g} modes are obtained in parallel polarization geometry due to their activation in monoclinic symmetry of the bright domains (*c.f.* sec. 4.3).

Mode	$YMnO_3$ LDC	$YMnO_3$ exp.	$YTiO_3$ exp.	$Y_{.63}Ca_{.37}TiO_3$
$A_g(7)$	104	151	145	
$A_g(5)$	147	188	168	
$A_g(2)$	223	288	273	
$A_g(6)$	304	323	314	294
$A_g(4)$	407	396	417	395
$A_g(3)$	466	497	446	458
$A_g(1)$	524	518	512	533
$B_{1g}(7)$	137	151	142	
$B_{1g}(5)$	162	220	219	
$B_{1g}(4)$	285	317	306	
$B_{1g}(6)$	393	341	328	
$B_{1g}(3)$	470	481	487	
$B_{1g}(2)$	583	537	521	
$B_{1g}(1)$	617	616	643	
$B_{2g}(5)$	145	178	151	
$B_{2g}(4)$	363	336	284	
$B_{2g}(3)$	390		366	342
$B_{2g}(2)$	476		452	495
$B_{2g}(1)$	610		678	638
$B_{3g}(5)$	181	205	162	
$B_{3g}(3)$	288	284	303	
$B_{3g}(4)$	342	384		
$B_{3g}(2)$	413		485	
$B_{3g}(1)$	593		644	593

Tab. B.1: Raman active mode assignments of orthorhombic $YMnO_3$, comparing it to Raman energies of $YTiO_3$. The Raman energies of $Y_{.63}Ca_{.37}TiO_3$ obtained from the fits are also listed.

C. RAMAN FITTING RESULTS

In the following the fitting results of the Raman spectra are completely listed. For the listed fitting parameters, the same letters as in eq. 3.10 are used. Energies and linewidths are given in cm^{-1}, amplitudes/ peak weights are given in arbitrary units. The q-parameter is dimensionless. Each table contains the temperature evolution of the lineshape parameters of a mode, obtained by the fits.

C.1 Bright domain results:

T (K)	ω_0	$\delta\omega_0$	Γ	$\delta\Gamma$	A	δA	q	δq
10	294.2	0.7	29.9	3.4	3110	450		
100	294.2	0.8	32.1	3.7	3260	490		
150	297.3	1.1	37.5	4.4	3300	580		
180	298.4	4.3	57.0	24.2	5330	7020		
220	299.3	1.6	43.8	3.7	3.2	2.1	-15.7	10.6
260	301.2	1.8	33.7	3.4	9.0	3.2	-4.6	1.7
296	301.8	1.0	35.3	2.6	16.6	1.6	-3.0	0.3

Tab. C.1: Lineshape: Lorentzian and Fano

T (K)	ω_0	$\delta\omega_0$	Γ	$\delta\Gamma$	A	δA
10	342.0	3.0	55.1	16.3	3170	1550
100	335.2	2.0	41.4	11.3	2200	900
150	339.4	3.8	52.9	20.4	2050	1170
180	341.7	6.6	16.8	4.2	357	5
220						
260						
296						

Tab. C.2: Lineshape: Lorentzian

T (K)	ω_0	$\delta\omega_0$	Γ	$\delta\Gamma$	A	δA	q	δq
10	394.6	1.6	38.0	2.2	17.1	11.4	-8.6	5.8
100	395.5	1.8	43.5	2.7	23.5	10.3	-6.1	2.9
150	393.9	1.3	46.7	2.7	13.0	6.1	-9.6	4.4
180	393.3	0.9	46.1	2.9	13.6	6.6	-7.9	4.2
220	395.0	1.3	49.7	2.5	23.6	3.5	-4.0	0.6
260	392.9	2.3	55.5	4.1	19.9	6.6	-4.3	1.6
296	393.8	1.7	58.9	4.1	31.6	5.2	-3.0	0.4

Tab. C.3: Lineshape: Fano

T (K)	ω_0	$\delta\omega_0$	Γ	$\delta\Gamma$	A	δA	q	δq
10	457.9	4.4	38.0	5.3	28.1	16.8	-2.3	1.5
100	458.8	5.5	47.6	6.3	31.7	22.4	-2.6	1.9
150	458.5	1.6	36.8	5.4	22.8	3.4	-2.0	0.2
180	458.7	4.6	42.4	6.7	20.1	5.8	-1.7	0.9
220	459.3	2.4	50.7	6.9	22.2	3.4	-1.8	0.3
260	458.9	4.0	40.2	7.0	16.6	3.9	-1.6	0.7
296	449.2	5.2	57.4	7.7	12.1	6.9	-3.8	2.8

Tab. C.4: Lineshape: Fano

T (K)	ω_0	$\delta\omega_0$	Γ	$\delta\Gamma$	A	δA
10	495.5	2.9	51.8	26.6	5770	7940
100	497.6	3.3	47.2	29.2	4570	7800
150	495.0	1.9	18.5	11.7	470	460
180						
220						
260						
296						

Tab. C.5: Lineshape: Lorentzian

T (K)	ω_0	$\delta\omega_0$	Γ	$\delta\Gamma$	A	δA
10	532.7	10.2	104.2	27.7	23660	11950
100	526.9	12.1	94.8	21.0	19660	10540
150	522.3	3.5	141.1	12.7	30080	3120
180	520.9	1.6	158.2	1.5	29900	600
220	519.4	3.7	173.7	21.7	28110	3580
260	527.6	11.3	250.3	68.7	34620	16030
296	546.6	10.6	247.6	16.6	33790	2520

Tab. C.6: Lineshape: Lorentzian

T (K)	ω_0	$\delta\omega_0$	σ	$\delta\sigma$	A	δA
10	593.8	0.5	18.5	0.8	3770	340
100	599.6	0.5	18.4	1.1	2770	360
150	603.1	0.7	27.1	1.8	4720	1010
180	600.4	6.7	26.2	2.2	2810	660
220	595.9	1.5	18.3	3.4	660	240
260	594.3	1.8	15.8	3.6	400	150
296	609.5	17.8	35.6	16.6	1190	2870

Tab. C.7: Lineshape: Gaussian

T (K)	ω_0	$\delta\omega_0$	σ	$\delta\sigma$	A	δA
10	637.8	0.7	53.5	0.9	41040	1470
100	638.8	0.8	56.0	0.9	47990	1580
150	645.0	1.5	53.1	1.3	33840	1530
180	644.6	1.0	54.2	1.5	23940	1840
220	639.6	1.5	57.6	1.9	16810	1090
260	642.1	1.7	54.5	3.4	9140	1350
296	651.6	22.2	48.3	13.2	4200	2970

Tab. C.8: Lineshape: Gaussian

T (K)	a	δa	b	δb
10	0.099	0.016	-83	25
100	0.147	0.022	-118	32
150	0.123	-	-100	-
180	0.093	0.016	-76	21
220	0.075	-	-65	-
260	0.014	0.026	-24	35
296	-0.008	-	-10	-

Tab. C.9: Baseline $a \cdot \omega + b$

T (K)	ω_0	$\delta\omega_0$	Γ	$\delta\Gamma$	A	δA	q	δq
10	310.1	0.2	13.2	0.3	49.4	4.8	-6.2	0.6
100	309.4	0.3	15.7	0.4	53.2	6.2	-4.9	0.6
150	307.9	0.4	19.5	0.7	58.9	6.7	-3.2	0.4
180	308.2	2.6	35.1	2.5	43.4	13.9	-1.8	0.7
220	307.1	1.3	31.3	2.8	26.1	2.4	-1.6	0.2
260	303.9	1.3	38.2	3.0	30.1	2.4	-1.6	0.2
296	302.3	1.2	38.3	2.8	29.1	2.8	-1.8	0.2

Tab. C.10: Lineshape: Fano

C.2 Dark domain results:

T (K)	ω_0	$\delta\omega_0$	Γ	$\delta\Gamma$	A	δA
10	336.3	0.7	30.3	3.3	3770	570
100	335.7	0.9	30.2	4.6	3240	740
150	333.6	2.0	36.5	10.8	2400	1200
180	335.8	3.9	37.2	24.7	1760	2710
220						
260						
296						

Tab. C.11: Lineshape: Lorentzian

T (K)	ω_0	$\delta\omega_0$	Γ	$\delta\Gamma$	A	δA	q	δq
10	387.5	0.1	20.1	0.3	108.7	6.7	-7.0	0.5
100	387.0	0.2	23.8	0.4	110.4	8.3	-5.8	0.5
150	384.6	0.3	30.2	0.4	73.1	8.5	-6.6	0.8
180	385.3	2.5	49.5	2.3	38.3	23.4	-5.3	3.4
220	394.5	3.9	58.3	5.7	55.7	21.9	-2.2	1.1
260	393.1	3.9	64.6	4.8	53.1	20.9	-2.3	1.1
296	392.9	4.1	67.5	4.8	53.8	21.0	-2.4	1.0

Tab. C.12: Lineshape: Fano

T (K)	ω_0	$\delta\omega_0$	Γ	$\delta\Gamma$	A	δA
10	419.1	3.8	38.1	11.0	5710	3940
100	422.2	7.9	44.3	20.8	6410	11210
150	422.7	2.0	32.1	7.8	3520	1780
180	431.9	6.0	51.6	28.2	4950	5610
220	429.2	4.0	46.4	31.7	3940	5750
260	434.5	5.3	54.5	31.7	5470	6940
296	428.9	3.2	38.4	20.7	2520	3000

Tab. C.13: Lineshape: Lorentzian

T (K)	ω_0	$\delta\omega_0$	Γ	$\delta\Gamma$	A	δA
10	437.0	3.2	37.1	5.3	5710	3270
100	437.6	14.3	54.2	8.6	6410	10910
150	442.9	4.8	42.8	7.8	3520	1750
180	452.8	3.1	25.9	17.4	1070	1830
220	452.3	3.4	28.5	13.4	1370	1640
260	455.8	3.2	24.4	20.7	740	1560
296	451.7	2.8	33.1	8.9	2150	1340

Tab. C.14: Lineshape: Lorentzian

T (K)	ω_0	$\delta\omega_0$	Γ	$\delta\Gamma$	A	δA	q	δq
10	558.3	0.9	31.2	1.8	25.3	1.4	-2.2	0.2
100	555.1	1.2	36.7	2.4	20.4	1.8	-2.9	0.3
150	554.2	1.4	34.3	2.8	13.7	1.7	-3.3	0.5
180	538.0	3.5	144.4	21.0	17860	4110		
220	534.6	8.4	211.1	56.6	25480	12200		
260	528.6	7.2	170.2	48.3	17200	8050		
296	530.7	10.0	199.2	72.6	22770	15620		

Tab. C.15: Lineshape: Fano and Lorentzian

T (K)	ω_0	$\delta\omega_0$	σ	$\delta\sigma$	A	δA
10						
100						
150						
180	606.8	2.7	24.5	6.1	953	710
220						
260						
296						

Tab. C.16: Lineshape: Gaussian

T (K)	ω_0	$\delta\omega_0$	σ	$\delta\sigma$	A	δA
10						
100						
150						
180	647.7	4.6	50.3	4.4	7970	1280
220	641.7	2.4	56.1	4.5	6110	1310
260	637.0	4.2	61.9	6.5	5590	1540
296	638.3	5.8	61.9	8.4	4740	1840

Tab. C.17: Lineshape: Gaussian

T (K)	a	δa	b	δb
10	0.347	0.006	-148	5
100	0.344	0.007	-156	7
150	0.095	0.008	-15	8
180	0.033	0.030	-30	37
220	-0.007	0.036	-20	55
260	-0.017	0.045	-11	54
296	-0.025	0.051	-12	64

Tab. C.18: Baseline $a \cdot \omega + b$

BIBLIOGRAPHY

[1] Dagotto E. Complexity in Strongly Correlated Electronic Systems. Science. 2005;309(5732):257–262. Available from: `http://www.sciencemag.org/content/309/5732/257.abstract`. 2

[2] Khomskii DI. Transition Metal Compounds. 1st ed. 9781107020177. CAMBRIDGE UNIVERSITY PRESS; 2014. 2, 8

[3] Imada M, Fujimori A, Tokura Y. Metal-insulator transitions. Rev Mod Phys. 1998 Oct;70:1039–1263. Available from: `http://link.aps.org/doi/10.1103/RevModPhys.70.1039`. 3, 5

[4] Morin FJ. Oxides Which Show a Metal-to-Insulator Transition at the Neel Temperature. Phys Rev Lett. 1959 Jul;3:34–36. Available from: `http://link.aps.org/doi/10.1103/PhysRevLett.3.34`. 3

[5] Kato K, Nishibori E, Takata M, Sakata M, Nakano T, Uchihira K, et al. The Metal-Insulator Transition in $Y_{1-x}Ca_xTiO_3$ Caused by Phase Separation. Journal of the Physical Society of Japan. 2002;71(9):2082–2085. Available from: `http://dx.doi.org/10.1143/JPSJ.71.2082`. 3, 6, 34, 35

[6] Tsubota M, Iga F, Nakano T, Uchihira K, Kura S, Takemura M, et al. Hole-doping and Pressure Effects on the Metal-Insulator Transition in Single Crystals of $Y_{1-x}Ca_xTiO_3$ ($0.37 \leq x \leq 0.41$). Journal of the Physical Society of Japan. 2003;72(12):3182–3188. Available from: `http://dx.doi.org/10.1143/JPSJ.72.3182`. 3, 6, 40

[7] Komarek AC, Reuther M, Lorenz T, Cousson A, Link P, Morgenroth W, et al. Evidence for charge and orbital order in the doped titanates RE_(1-x)Ca_xTiO_3 (RE=Y, Er, Lu). ArXiv e-prints. 2011 Sep;. 3, 6, 7, 35

[8] Komarek AC. Complex ordering phenomena in transition metal oxides and oxyhalides. Universität zu Köln; 2009. 4, 5, 6, 7, 22, 34, 35, 36, 41

[9] Taguchi Y, Tokura Y, Arima T, Inaba F. Change of electronic structures with carrier doping in the highly correlated electron system $Y_{1-x}Ca_xTiO_3$. Phys Rev B. 1993 Jul;48:511–518. Available from: `http://link.aps.org/doi/10.1103/PhysRevB.48.511`. 5, 28

[10] MacLean DA, Ng HN, Greedan JE. Crystal structures and crystal chemistry of the {RE-TiO3} perovskites: {RE} = La, Nd, Sm, Gd, Y. Journal of Solid State Chemistry. 1979;30(1):35 – 44. Available from: `http://www.sciencedirect.com/science/article/pii/0022459679901270`. 5

[11] Glazer AM. The classification of tilted octahedra in perovskites. Acta Crystallographica Section B. 1972 Nov;28(11):3384–3392. Available from: `http://dx.doi.org/10.1107/S0567740872007976`. 5

[12] Goral JP, Greedan JE, MacLean DA. Magnetic behavior in the series $La_xY_{1-x}TiO_3$. Journal of Solid State Chemistry. 1982;43(3):244 – 250. Available from: `http://www.sciencedirect.com/science/article/pii/0022459682902365`. 5

[13] Goodenough JB. Theory of the Role of Covalence in the Perovskite-Type Manganites $[La, M(II)]MnO_3$. Phys Rev. 1955 Oct;100:564–573. Available from: `http://link.aps.org/doi/10.1103/PhysRev.100.564`. 5

[14] Kanamori J. Superexchange interaction and symmetry properties of electron orbitals. Journal of Physics and Chemistry of Solids. 1959;10(2):87 – 98. Available from: `http://www.sciencedirect.com/science/article/pii/0022369759900617`.

[15] Anderson PW. Antiferromagnetism. Theory of Superexchange Interaction. Phys Rev. 1950 Jul;79:350–356. Available from: `http://link.aps.org/doi/10.1103/PhysRev.79.350`. 5

[16] Nakao H, Kodama S, Kiyoto K, Murakami Y, Tsubota M, Iga F, et al. Resonant X-ray Scattering Study at Y K-edge in Y1-xCaxTiO3. Journal of the Physical Society of Japan. 2006;75(9):094706. Available from: `http://dx.doi.org/10.1143/JPSJ.75.094706`. 5, 6

[17] Matsuhata H, Iga F, Tsubota M, Nakano T, Takabatake T, Kato K. Phase separation in $Y_{1-x}Ca_xTiO_3$ associated with the insulator-to-metal transition: Observation by transmission electron microscopy. Phys Rev B. 2004 Oct;70:134109. Available from: `http://link.aps.org/doi/10.1103/PhysRevB.70.134109`. 6, 8, 9, 27, 34, 35, 40

[18] Kim KH. Colossal Magnetoresistve Manganites. 1st ed. Chatterji T, editor. 978-90-486527-8. KLUWER ACADEMIC PUBLISHERS; 2004. 8, 9

[19] Moreo A, Mayr M, Feiguin A, Yunoki S, Dagotto E. Giant Cluster Coexistence in Doped Manganites and Other Compounds. Phys Rev Lett. 2000 Jun;84:5568–5571. Available from: `http://link.aps.org/doi/10.1103/PhysRevLett.84.5568`. 9

[20] Ahn KH, Seman TF, Lookman T, Bishop AR. Role of complex energy landscapes and strains in multiscale inhomogeneities in perovskite manganites. Phys Rev B. 2013 Oct;88:144415. Available from: `http://link.aps.org/doi/10.1103/PhysRevB.88.144415`. 9, 10

[21] Podzorov V, Kim BG, Kiryukhin V, Gershenson ME, Cheong SW. Martensitic accommodation strain and the metal-insulator transition in manganites. Phys Rev B. 2001 Sep;64:140406. Available from: `http://link.aps.org/doi/10.1103/PhysRevB.64.140406`. 9

[22] Lu WJ, Sun YP, Zhao BC, Zhu XB, Song WH. Inhomogeneous strain and phase coexistence in $Bi_{0.4}Ca_{0.6}MnO_3$. Phys Rev B. 2006 Jun;73:214409. Available from: `http://link.aps.org/doi/10.1103/PhysRevB.73.214409`. 9

[23] Hayes W, Loudon R. Scattering of light by crystals. 1st ed. 0-471-03191-7. John Wiley and Sons, Inc.; 1978. 11, 12

[24] Pinczuk A, Burstein E, Martin RM, Falicov LM, Klein MV, Brodsky MH, et al. Light Scattering in Solids. 2nd ed. Cardona M, editor. 978-3-540-11913-5. Springer-Verlag Berlin Heidelberg; 1983. 11, 15

[25] Kuzmany H. Solid-State Spectroscopy. 2nd ed. 978-3-642-01478-9. Springer-Verlag Berlin Heidelberg; 2009. 13, 15

[26] Dresselhaus MS, Dresselhaus G, Jorio A. Group Theory, Application to the Physics of Condensed Matter. 1st ed. 978-3-540-32897-1. Springer-Verlag Berlin Heidelberg; 2008. 13, 14

[27] Poulet H, Mathieu JP. Vibration Spectra and Symmetry of Crystals. 1st ed. 978-0677301808. Gordon an Breach Science Publishers Ltd; 1976. 14

[28] Kroumova E, Aroyo MI, Perez-Mato JM, Kirov A, Capillas C, Ivantchev S, et al. Bilbao Crystallographic Server : Useful Databases and Tools for Phase-Transition Studies. Phase Transitions. 2003;76(1-2):155–170. Available from: `http://dx.doi.org/10.1080/0141159031000076110`. 14, 15

[29] Kovaleva NN, Boris AV, Capogna L, Gavartin JL, Popovich P, Yordanov P, et al. Dipole-active optical phonons in $YTiO_3$: Ellipsometry study and lattice-dynamics calculations. Phys Rev B. 2009 Jan;79:045114. Available from: `http://link.aps.org/doi/10.1103/PhysRevB.79.045114`. 14

[30] Fano U. Effects of Configuration Interaction on Intensities and Phase Shifts. Phys Rev. 1961 Dec;124:1866–1878. Available from: `http://link.aps.org/doi/10.1103/PhysRev.124.1866`. 15

[31] Mialitsin A, Fluegel B, Ptak A, Mascarenhas A. Mechanism of asymmetric lineshape broadening in $GaAs_{1-x}N_x$ Raman spectra. Phys Rev B. 2012 Jul;86:045209. Available from: `http://link.aps.org/doi/10.1103/PhysRevB.86.045209`. 15

[32] Tsurui T, Ogita N, Udagawa M, Tsubota M, Iga F. Raman scattering investigation of $Y_{1-x}Ca_xTiO_3$. Phys Rev B. 2004 Jan;69:024102. Available from: `http://link.aps.org/doi/10.1103/PhysRevB.69.024102`. 20, 21, 27, 30, 40

[33] Katsufuji T, Tokura Y. Anomalous variation of phonon Raman intensities near the metal-to-Mott-insulator transition in titanium oxide systems. Phys Rev B. 1994 Jul;50:2704–2707. Available from: `http://link.aps.org/doi/10.1103/PhysRevB.50.2704`. 20

[34] Komarek AC. Strukturuntersuchungen an Titanaten. Universit . 23

[35] Tsubota M, Iga F, Uchihira K, Nakano T, Kura S, Takabatake T, et al. Coupling between Orbital and Lattice Degrees of Freedom in $Y_{1-x}Ca_xTiO_3$ ($0 < x \leq 0.37$): A Resonant X-ray Scattering Study. Journal of the Physical Society of Japan. 2005;74(12):3259–3266. Available from: `http://dx.doi.org/10.1143/JPSJ.74.3259`. 27

[36] Ritchie RH. Plasma Losses by Fast Electrons in Thin Films. Phys Rev. 1957 Jun;106:874–881. Available from: `http://link.aps.org/doi/10.1103/PhysRev.106.874`. 28

[37] Khomskii DI. Basic Aspects of the Quantum Theory of Solids. 1st ed. 978-0-521-83521-3. CAMBRIDGE UNIVERSITY PRESS; 2010. 28

[38] Kumagai K, Suzuki T, Taguchi Y, Okada Y, Fujishima Y, Tokura Y. Metal-insulator transition in $La_{1-x}Sr_xTiO_3$ and $Y_{1-x}Ca_xTiO_3$ investigated by specific-heat measurements. Phys Rev B. 1993 Sep;48:7636–7642. Available from: `http://link.aps.org/doi/10.1103/PhysRevB.48.7636`. 28

[39] Iliev MN, Abrashev MV, Lee HG, Popov VN, Sun YY, Thomsen C, et al. Raman spectroscopy of orthorhombic perovskitelike $YMnO_3$ and $LaMnO_3$. Phys Rev B. 1998 Feb;57:2872–2877. Available from: `http://link.aps.org/doi/10.1103/PhysRevB.57.2872`. 31, 44

[40] Abrashev MV, Bäckström J, Börjesson L, Popov VN, Chakalov RA, Kolev N, et al. Raman spectroscopy of $CaMnO_3$: Mode assignment and relationship between Raman line intensities and structural distortions. Phys Rev B. 2002 Apr;65:184301. Available from: `http://link.aps.org/doi/10.1103/PhysRevB.65.184301`. 32

[41] Sugai S, Kikuchi A, Mori Y. Raman scattering of orbital waves in $YTiO_3$. Phys Rev B. 2006 Apr;73:161101. Available from: `http://link.aps.org/doi/10.1103/PhysRevB.73.161101`. 31, 32, 44

[42] Irwin JC, Chrzanowski J, Franck JP. Oxygen isotope effect on the vibrational modes of $La_{1-x}Ca_xMnO_3$. Phys Rev B. 1999 Apr;59:9362–9371. Available from: `http://link.aps.org/doi/10.1103/PhysRevB.59.9362`. 37

[43] Lee JD, Min BI. Polaron transport and lattice dynamics in colossal-magnetoresistance manganites. Phys Rev B. 1997 May;55:12454–12459. Available from: `http://link.aps.org/doi/10.1103/PhysRevB.55.12454`. 37